



1

2

**DALROMS-NWA12 v1.0, a coupled circulation-ice-  
biogeochemistry modelling system for the northwest Atlantic**

4

**Ocean: Development and validation**

5

6 Kyoko Ohashi<sup>1</sup>, Arnaud Laurent<sup>1</sup>, Christoph Renkl<sup>1</sup>, Jinyu Sheng<sup>1</sup>, Katja Fennel<sup>1</sup>, Eric Oliver<sup>1</sup>

7

<sup>1</sup>Department of Oceanography, Dalhousie University, Halifax, NS B3H 4R2 Canada

8

9 *Correspondence to:* Kyoko Ohashi (kyoko.ohashi@dal.ca)

10

11

12



13 **Abstract.** This study presents DalROMS-NWA12 v1.0, a coupled ocean circulation-sea ice-  
14 biogeochemistry modelling system for the northwest Atlantic Ocean (NWA) in which the  
15 circulation and biogeochemistry modules are based on ROMS (Regional Ocean Modeling  
16 System). The circulation module is coupled to a sea ice module based on the Community Ice  
17 Code (CICE), and the physical ocean state simulated by the circulation module drives the  
18 biogeochemical module. Study of the biological carbon pump in the NWA is one of the main  
19 intended applications of this model. Global atmospheric and ocean reanalyses are used  
20 respectively to force DalROMS-NWA12 at the sea surface and as part of its lateral boundary  
21 input. The modelling system is also forced by tides, riverine freshwater input, and continental  
22 runoff. The physical ocean state and sea ice from two simulations of the period 2015–2018, with  
23 and without nudging of the simulated temperature and salinity towards a blend of observations  
24 and reanalysis, are examined in this study. Statistical comparisons between model results and  
25 observations or reanalyses show the control (nudged) simulation outperforms the prognostic (un-  
26 nudged) simulation in reproducing the paths of the Gulf Stream and the West Greenland Current,  
27 as well as propagation of the estuarine plume in the Gulf of St. Lawrence. The prognostic  
28 simulation performs better in simulating the sea ice concentration. The biogeochemical module,  
29 which is run only in the control simulation, performs reasonably well in reproducing the  
30 observed spatiotemporal variations of oxygen, nitrate, alkalinity, and total inorganic carbon. To  
31 examine the effects of tides and sea ice on the physical fields in the study area, results of  
32 simulations from which either component is absent are compared to results of the prognostic  
33 simulation. In the absence of tides, Ungava Bay in summer experiences a simulated surface  
34 salinity that is higher by up to  $\sim 7$  than in the simulation with tides, as well as changes in  
35 horizontal distributions of surface temperature and sea ice. Without coupling to the sea ice  
36 module, the circulation module produces summertime sea surface temperatures that are higher by  
37 up to  $\sim 5^{\circ}\text{C}$  in Baffin Bay.



## 38 **1 Introduction**

39 The northwest North Atlantic Ocean (hereafter NWA) is characterized by interactions among  
40 physical and biogeochemical processes that affect the global atmosphere-ocean system. Air-to-  
41 sea flux of CO<sub>2</sub> per unit area is estimated to be largest in the world in the Atlantic Ocean north of  
42 50° N, due to factors such as strong winds in winter and high primary production in spring  
43 (Takahashi et al., 2009). The sinking of particles formed during primary production has the effect  
44 of transporting atmospheric CO<sub>2</sub> to the deep ocean and is referred to as the biological carbon  
45 pump (BCP; Volk and Hoffert, 1985). The BCP is influenced by various physical processes over  
46 an annual cycle. The presence of sea ice in winter can, on one hand, drive upward transport of  
47 nutrients through brine rejection-induced vertical mixing (Jin et al., 2018) but on the other hand  
48 can reduce wind-induced mixing (Rainville et al., 2011) and attenuate the solar radiation  
49 (Legendre et al., 1992) by isolating the water column from the atmosphere. Seasonal changes of  
50 the mixed layer depth is another physical process that governs the BCP. Shoaling of the layer in  
51 spring, driven by freshwater input from runoff and sea ice, promotes primary production (Wu et  
52 al., 2007 and 2008; Frajka-Williams and Rhines, 2010), while deepening of the layer in winter  
53 can result in entrainment of dissolved inorganic carbon and respiratory CO<sub>2</sub> that had been in  
54 shallow sub-surface waters (Körtzinger et al., 2008). In the Labrador Sea, deep convection in  
55 winter is thought to be an additional pathway for removal of carbon from near-surface waters  
56 (Tian et al., 2004).

57 Several field programs have been conducted to quantify the major processes at work in the  
58 NWA, such as the Labrador Sea Deep Convection Experiment (The Lab Sea Group, 1998),  
59 which focused on atmospheric and physical oceanographic processes, and the Atlantic Zone  
60 Monitoring Program (Pepin et al., 2005) and its off-shelf counterpart (e.g., Yashayaev and Loder,  
61 2017), which have made regular shipboard measurements of physical and biogeochemical (BGC)  
62 fields at fixed locations. Simultaneous measurements of physical and BGC fields at moorings  
63 (e.g., Martz et al., 2009; Strutton et al., 2011) and by profiling floats (e.g., Yang et al., 2020;  
64 Wang and Fennel 2022) have expanded the coverage of observations, which is crucial given the  
65 spatiotemporal variability in the processes that govern the BCP (Garçon et al., 2001).



66 Processed-based numerical models can complement observations of oceanic processes by  
67 providing four-dimensional estimates of relevant fields and by enabling experiments in which the  
68 effects of key inputs are isolated or the future state of oceans under various climate scenarios are  
69 simulated (Fennel et al., 2022). Early numerical studies of the NWA using coupled ocean  
70 circulation-sea ice models focused mainly on specific processes, such as climatological sea ice  
71 conditions (Mysak et al., 1991), sea ice variabilities on the interannual (Ikeda et al., 1996) and  
72 intra-seasonal (Yao et al., 2000) time scales, and changes in sea ice and mixed layer properties  
73 under different atmospheric conditions (Tang et al., 1999). As process-based numerical models  
74 grew in complexity they yielded new insights, such as the role of sea ice's heat capacity in the  
75 timing of ice melt (Zhang et al., 2004). Advances in computational power have led to realistic  
76 simulations spanning a decade or more covering limited areas, such as the Canadian Arctic  
77 Archipelago and Davis Strait (Lu et al., 2014) or the Labrador and Newfoundland Shelves (Ma et  
78 al., 2016). Other ocean-ice models of areas within the NWA include that of the Gulf of St.  
79 Lawrence and surrounding waters (Urrego-Blanco and Sheng, 2014; Wang et al., 2020), Hudson  
80 Bay (Saucier et al., 2004), and the Labrador Sea (Pennelly and Myers, 2020). Canadian  
81 government agencies have developed coupled ocean-ice or atmosphere-ocean-ice models to  
82 support activities such as hazard management, with domains ranging from the regional (e.g.,  
83 Smith et al., 2013 for the Gulf of St. Lawrence) to basin-wide (Dupont et al., 2015; Wang et al.,  
84 2018). Other modelling studies have focused on hydrodynamics in coastal and shelf waters of the  
85 NWA, such as Han et al. (1997) for the Scotian Shelf, Wu et al. (2012) for the area between the  
86 Gulf of Maine and Baffin Bay, and Chen and He (2015) for the Mid-Atlantic Bight and the Gulf  
87 of Maine.

88 As for coupled physical-BGC modelling studies, three-dimensional models with high resolutions  
89 have generally focused on the shelf and slope areas of the NWA. Pei (2022) used a simple  
90 oxygen model to study seasonal changes in dissolved oxygen over the Scotian Shelf, while more  
91 complex models have been used to study the biogeochemistry and plankton dynamics of the  
92 Scotian Shelf and surrounding waters (Laurent et al., 2021, Rutherford and Fennel, 2022) and the  
93 Gulf of St. Lawrence (LeFouest et al., 2010; Lavoie et al., 2021). Ross et al. (2023) developed a  
94 coupled physical-BGC model for the North Atlantic Ocean from the Caribbean Sea to the  
95 southern Labrador Sea, designed primarily for marine resource management.



96 As coupled simulations that include more processes and cover larger extents of space and time  
97 become feasible, they are expected to enhance our understanding of how the ocean functions as  
98 an integrated system, as well as how this system might change under various scenarios of the  
99 future climate. In this study, we present and assess a coupled ocean circulation-sea ice-BGC  
100 model that has been developed recently with the primary goal of studying the interactions  
101 between physical and BGC processes in the NWA, including the BCP. Advantages of this  
102 model's configuration include: (a) a domain that spans the area from the Mid-Atlantic Bight to  
103 Baffin Bay, allowing for a wide range of oceanographic processes that can be examined; (b) a  
104 horizontal grid size of  $O(\text{km})$  that decreases with latitude, such that the first baroclinic Rossby  
105 radius of deformation (Chelton et al., 1998) is spanned by about four grid boxes everywhere; (c)  
106 the use of a terrain-following vertical coordinate system, which can produce more realistic near-  
107 bottom vertical mixing and bottom boundary layer structures than the step-wise bottom  
108 topography of z-level grids (Ezer and Mellor, 2004); (d) the inclusion of tides (as one of the  
109 model inputs) and sea ice (through coupling between the circulation and sea ice modules), both  
110 of which are important elements of the ocean system in this region, and (e) the inclusion of a  
111 BGC module, which enables the study of how processes such as the BCP are driven by the  
112 coupled ocean circulation-sea ice system. This paper provides an assessment of the coupled  
113 model's performance as well as sensitivity studies designed to elucidate the role of two physical  
114 processes, tides and sea ice. The components of the coupled model and the simulations are  
115 described in the next section. In Sect. 3, the results of two simulations, with and without nudging  
116 of the temperature and salinity towards a blend of observations and reanalysis (referred to  
117 respectively as the control and prognostic simulations), are described and quantitatively  
118 compared to observations or reanalysis. In Sect. 4, the roles of tides and sea ice in the physical  
119 fields of the NWA are examined by comparing the results of two additional simulations, one  
120 without tidal forcing and the other without the simulation of sea ice, to results of the prognostic  
121 simulation described in Sect. 3. A summary of our findings is presented in the concluding  
122 section.



## 123 2 Model setup and forcing

124 The coupled circulation-sea ice-BGC modelling system used in this study consists of three  
125 modules: an ocean circulation module based on ROMS (Regional Ocean Modeling System,  
126 version 3.9; Haidvogel et al., 2008), a sea ice module based on CICE (Community Ice Code,  
127 version 5.1; Hunke et al., 2015), and a BGC module within ROMS based on the work of Fennel  
128 et al. (2006, 2008) with updates as described by Laurent et al. (2021). The circulation and sea ice  
129 modules are coupled using the software MCT (Model Coupling Toolkit, version 2.10; Jacob et  
130 al., 2005; Larson et al., 2005) in a manner similar to Kristensen et al. (2017). Yang et al. (2023)  
131 found good agreement between simulated and observed values of tides and storm surges  
132 simulated by a barotropic version of the ocean circulation module.

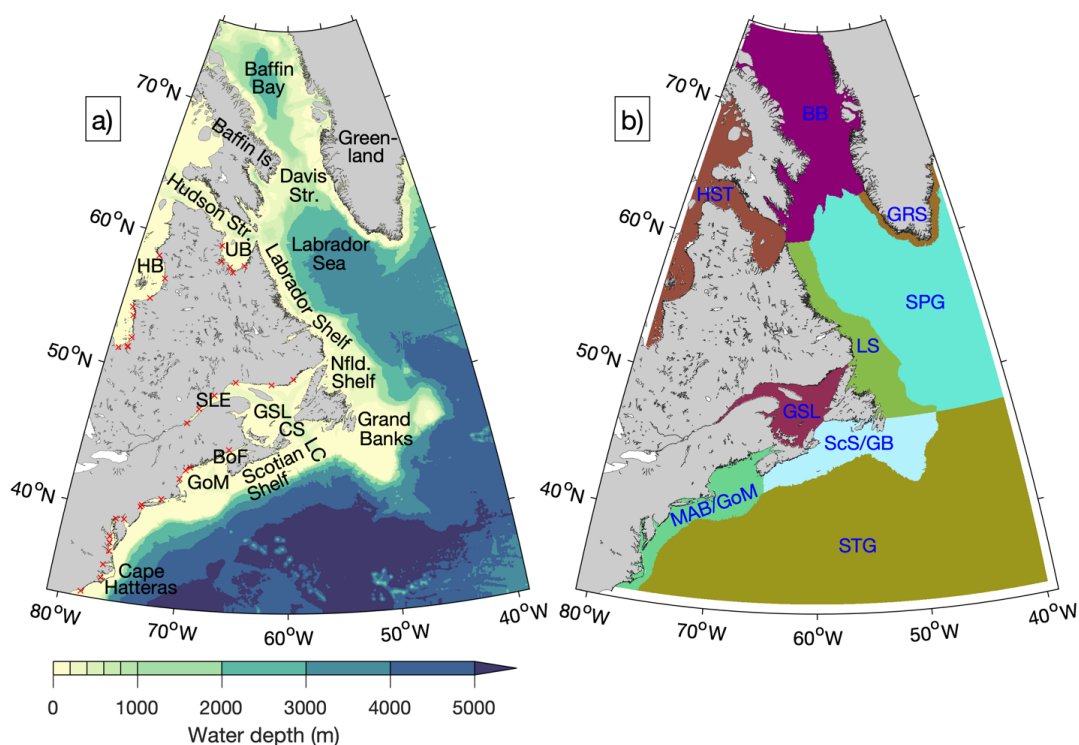
133 ROMS is a three-dimensional (3D) numerical circulation model with a free surface and the  
134 terrain-following S-coordinate system (originally developed by Song and Haidvogel (1994)) in  
135 the vertical. The vertical layers are placed more densely near the surface and bottom in deep  
136 waters, and more uniformly in shallow waters. In this study ROMS has 40 vertical layers, whose  
137 configuration is described in Appendix A. ROMS and CICE use the same horizontal grid and  
138 bathymetry, with the domain covering the area between  $\sim 81^\circ$  W and  $\sim 39^\circ$  W and between  $\sim 33.5^\circ$   
139 N and  $\sim 76^\circ$  N (Fig. 1a). The grid resolution in the east-west direction is  $1/12^\circ$ , resulting in grid  
140 box dimensions of  $\sim 8$  km on each side near the grid's southern boundary and  $\sim 2$  km on each side  
141 near the northern boundary.

142 The model bathymetry is derived from the  $1/240^\circ$ -resolution data set GEBCO\_2019 (GEBCO  
143 Compilation Group, 2019). After the GEBCO data were linearly interpolated onto the model  
144 grid, the Shapiro filter (Shapiro, 1975) was applied to seamounts in deep waters from  $\sim 67.5^\circ$  W  
145 to  $\sim 42^\circ$  W and from  $\sim 34^\circ$  N to  $\sim 48^\circ$  N to reduce currents caused by spurious pressure gradients.  
146 No other smoothing was applied to the bathymetry. To avoid model instability caused by strong  
147 currents entering the model domain at an angle, the model bathymetry and land-sea mask in the  
148 first four grid boxes from each lateral boundary were set to the same values as in the fifth grid  
149 box from the boundary.

150 The advection schemes used in ROMS for physical fields are: (a) the third-order upstream  
151 scheme for horizontal advection of physical tracers and 3D momentum and (b) the fourth-order



152 centered scheme for horizontal advection of two-dimensional momentum and for vertical  
 153 advection of physical tracers and 3D momentum. The horizontal eddy viscosity and diffusivity  
 154 are set to zero. Vertical mixing is parameterized using the “2.5-level” scheme of Mellor and  
 155 Yamada (1982) with modifications as described by Allen et al. (1995). The time step is 6 seconds  
 156 for the external (barotropic) mode and 120 seconds for the internal (baroclinic) mode.



157

158 **Figure 1. (a)** Model domain and bathymetry. Locations of river mouths are indicated by red X marks. Abbreviations  
 159 are used for: Island (Is), Strait (Str.), Hudson Bay (HB), Ungava Bay (UB), Newfoundland (Nfd.), St. Lawrence  
 160 Estuary (SLE), Gulf of St. Lawrence (GSL), Cabot Strait (CS), Laurentian Channel (LC), Bay of Fundy (BoF), and  
 161 Gulf of Maine (GoM). **(b)** Regions in which metrics of model performance are calculated. The regions are: GRS  
 162 (Greenland Shelf), HST (Hudson Strait), BB (Baffin Bay), LS (Labrador Shelf), SPG (Subpolar Gyre), GSL (Gulf of  
 163 St. Lawrence), ScS/GB (Scotian Shelf/Grand Banks), MAB/GoM (Mid-Atlantic Bight/Gulf of Maine), and STG  
 164 (Subtropical Gyre). Areas within 10 grid points of lateral boundaries are excluded from the error metric calculations.

165 Atmospheric fields used to drive the coupled model are derived from the hourly reanalysis data  
 166 set ERA5 (Hersbach et al., 2018) which has a horizontal grid spacing of  $1/4^\circ$ . Within ROMS, the  
 167 bulk flux scheme of Fairall et al. (1996a, 1996b) is used to calculate the surface fluxes of heat



168 and fresh water. Lateral open boundary conditions are specified using the explicit scheme of  
169 Chapman (1985) for sea surface elevation, the Shchepetkin scheme (Mason et al., 2010) for  
170 depth-averaged currents, and the adaptive scheme of Marchesiello et al. (2001) for depth-varying  
171 currents and all tracers. In the adaptive boundary condition, the nudging time scale is three days  
172 for inflow and 360 days for outflow. The values of currents, temperature, salinity, and sea surface  
173 elevation specified at the lateral boundaries are derived from the daily reanalysis data set  
174 GLORYS12V1 (hereafter GLORYS; Lellouche et al., 2021) which has a horizontal grid size of  
175  $1/12^\circ$ . The lateral boundary conditions of currents, temperature, and salinity are supplemented by  
176 nudging the simulated values near boundaries towards GLORYS values. The nudging time scale  
177 is three days at the grid point closest to a lateral boundary and decreases linearly to zero over ten  
178 grid points moving away from the boundary. Tidal elevation and currents are specified at the  
179 lateral boundaries from the global tidal model solution TPXO9v2a (an updated version of the  
180 model by Egbert and Erofeeva (2002)), with a horizontal grid size of  $1/6^\circ$  and 15 tidal  
181 constituents.

182 Riverine freshwater input from 35 rivers (Table 1) is specified as volume flux through the bottom  
183 of a model grid cell. Each river is represented by a channel normal to the model's coastline, at  
184 the head of which the surface elevation, vertical velocity, and tracer values are adjusted  
185 according to the river discharge. The river water has a salinity of 0.4 and a temperature equal to  
186 that of the GLORYS sea surface temperature at the grid point closest to the river mouth. For the  
187 St. Lawrence River, we use the monthly-mean discharge at Quebec City estimated by the St.  
188 Lawrence Global Observatory (2023) using the regression model of Bourgault and Koutitonsky  
189 (1999). For all other rivers, we use the monthly-mean data set of Dai (2017) that was updated in  
190 May 2019, substituting climatological values calculated over the period 1900–2018 for months  
191 with no data. Freshwater flux across coastlines due to the melting of ice and snow over land is  
192 specified as an addition to the sea surface height and the surface freshwater flux at the  
193 appropriate model grid boxes. This freshwater flux is derived from the monthly data set of  
194 Bamber et al. (2018), who combined satellite observations of glaciers with the output of a  
195 regional climate model. A monthly climatology of this data set, which covers the period 1958–  
196 2016, is used in simulations of the period after December 2016. Both the riverine and continental  
197 freshwater fluxes are converted to “pseudo-means” (monthly means that are adjusted such that



198 daily-mean values temporally interpolated from them, when summed over a month, results in the  
 199 true monthly means) following Killworth (1996).

200

201 **Table 1.** Names and discharge locations of rivers in the coupled model.

<b>River</b>	<b>Lon.</b> (° W)	<b>Lat.</b> (° N)	<b>River</b>	<b>Lon.</b> (° W)	<b>Lat.</b> (° N)
Innuksuac	78.06	58.42	Saguenay	69.72	48.06
Nastapoca	76.56	56.91	St. Lawrence	70.81	46.94
Great Whale	77.81	55.28	Saint John	66.14	45.32
Roggan	79.56	54.37	Androscoggin	69.89	43.78
La Grande + Sakami	79.22	53.78	Saco	70.31	43.54
Eastmain	78.72	52.23	Merrimack +	70.81	42.87
Rupert	78.89	51.56	Pemigewasset		
Nottaway	78.89	51.51	Connecticut	72.31	41.26
Harricana	79.89	51.30	Hudson	74.06	40.63
Arnaud	69.64	60.04	Passaic (Ramapo)	74.14	40.50
Leaf	69.39	58.90	Delaware + Beaver Kill	75.47	39.42
Koksoak (Caniapiscau + Mélézes)	68.14	58.55	Susquehanna	76.22	39.35
False + Whale	67.64	58.20	Potomac	76.47	38.05
George	66.14	58.77	Rapidan +	76.39	37.59
Petit Mécatina	59.39	50.62	Rappahannock		
Natashquan	61.89	50.19	James	76.31	36.99
Moisie	65.97	50.24	Roanoke	76.64	35.99
Manicouagan +	68.22	49.17	Neuse (Contentnea)	76.64	35.04
Outardes			Cape Fear	78.14	33.87

202 The sea ice model CICE consists of four main components: (a) a thermodynamic component that  
 203 calculates local growth or decay of sea ice due to snowfall and heat fluxes (Bitz and Lipscomb,  
 204 1999; Briegleb and Light, 2007); (b) a dynamic component that calculates the material properties



205 of the ice (Hunke and Dukowicz, 1997; Bouillon et al., 2013); (c) a transport component that  
206 calculates the horizontal advection of the ice (Lipscomb and Hunke, 2004); and (d) a component  
207 that calculates the distribution of ice among thickness categories due to ridging and mechanical  
208 processes (Hunke et al., 2015). There are seven ice layers and five ice thickness categories. We  
209 implemented the clamped boundary condition, in which GLORYS-derived values of sea ice  
210 concentration (as a fraction of the model grid box area) and thickness are specified at the model's  
211 lateral open boundaries. The sea ice specified at the lateral boundaries is uniformly covered with  
212 snow of 0.2-m thickness. The time step in CICE is 1200 seconds.

213 Coupling between ROMS and CICE via MCT occurs every 1200 seconds, equivalent to every 10  
214 internal time steps in ROMS and every time step in CICE. At each coupling step, ROMS sends  
215 CICE the ERA5-derived atmospheric fields that drive both modules, as well as ROMS-simulated  
216 values of currents, sea surface tilt, and sea-surface values of temperature and salinity. CICE  
217 sends ROMS the ice-attenuated value of shortwave radiation and ice-ocean fluxes of stress, heat,  
218 and salt or freshwater.

219 The BGC module includes the nitrogen cycle (Fennel et al., 2006), the carbonate system (Fennel  
220 et al., 2008), and oxygen (Fennel et al., 2013). Particulate organic matter variables  
221 (phytoplankton, zooplankton, and detritus) are split into small and large size classes, and rates of  
222 biological processes are temperature-dependent (Laurent et al., 2021). The HSIMT advection  
223 scheme (Wu and Zhu, 2010), which ensures no spurious negative values occur, is used for both  
224 horizontal and vertical advection of BGC tracers. Initial and boundary conditions for nitrate,  
225 phosphate, dissolved inorganic carbon, alkalinity, and oxygen are interpolated from the  
226 climatology of GLODAP (Global Ocean Data Analysis Project; Lauvset et al., 2021) and set to a  
227 small constant value for all other biogeochemical variables.

228 Four simulations will be examined in this paper. In the control simulation (hereafter Ctrl), the  
229 ocean temperature and salinity at all grid points are nudged with a restoring time scale of 60 days  
230 toward the monthly data set of in situ observations known as CORA (CORiolis dataset for Re-  
231 Analysis; Cabanes et al., 2013) above the 2000-m depth and GLORYS below 2000 m (where  
232 CORA data are not available). The control simulation includes biogeochemistry. The second  
233 simulation is a prognostic one (hereafter Prog), i.e., without any nudging of the simulation. There



234 are three reasons for presenting these simulations: 1) the ways in which either simulation  
 235 outperforms the other can shed light on potential ways in which the model can be improved; 2)  
 236 Ctrl, by including nudging of the temperature and salinity, produces a physical state of the ocean  
 237 that is generally realistic and acts as a foundation for the biogeochemical simulation; and 3) this  
 238 modelling system is being used in regional climate simulations (Renkl et al., in prep.), and the  
 239 lack of an option to nudge simulations of future conditions necessitates assessment of a  
 240 prognostic simulation. The performances of Ctrl and Prog will be evaluated in the next section.  
 241 Two more simulations are carried out for the sensitivity studies discussed in Sect. 4. Both are  
 242 identical to Prog but one is made without the specification of tidal elevation and currents at the  
 243 lateral boundaries (hereafter NoTides) and the other is made without coupling of ROMS to CICE  
 244 (hereafter NoIce). Configurations of the simulations are summarized in Table 2. All simulations  
 245 are made from 1 September 2013 to 31 December 2018 and are initialized with an ice-free ocean  
 246 in which the ocean’s state consists of GLORYS fields for 1 September 2013 interpolated to the  
 247 model grid. The simulation results of January 2015 onwards (December 2014 onwards in the  
 248 case of seasonal averages) will be discussed in the following sections.

249 **Table 2.** Descriptions of the simulations discussed in this study.

<b>Simulation name</b>	<b>Description</b>	<b>Temperature &amp; salinity nudging</b>	<b>Tidal forcing at lateral boundaries</b>	<b>Coupling to sea ice model</b>
Ctrl	Control	On	On	On
Prog	Prognostic	<b>Off</b>	On	On
NoTides	No tidal forcing	<b>Off</b>	<b>Off</b>	On
NoIce	No sea ice simulation	<b>Off</b>	On	<b>Off</b>

250 **3 Model results and evaluation**

251 **3.1 Simulated currents, temperature, and salinity**

252 We first examine four-year (1 January 2015–31 December 2018) averages of currents, salinity,  
 253 and temperature produced by DalROMS-NWA12 v1.0 in runs Ctrl and Prog (Figs. 2 and 3  
 254 respectively). Both model runs reproduce the major features of the circulation in this region.  
 255 They include: (a) the East and West Greenland Currents forming a clockwise flow around the

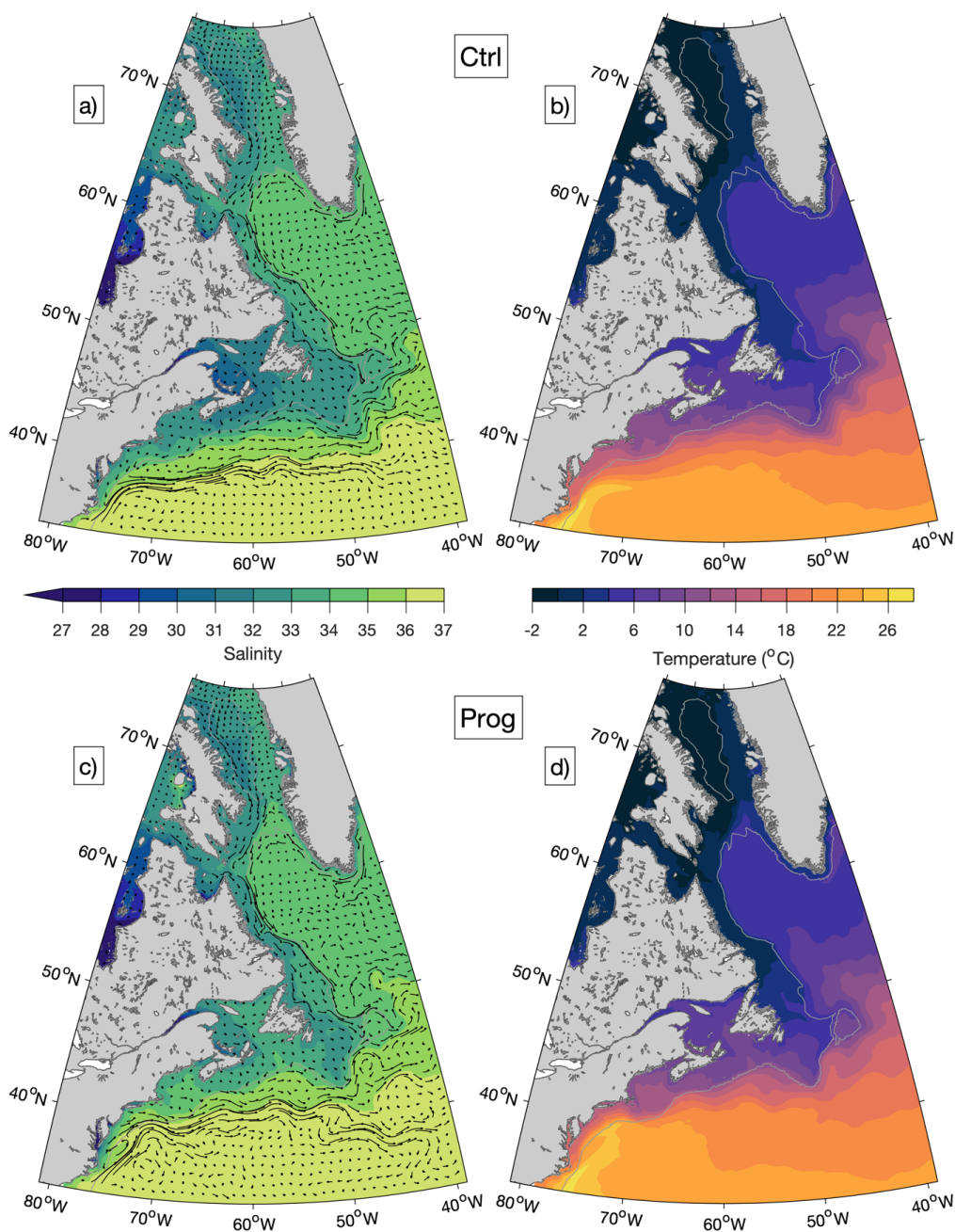


256 southern tip of Greenland; (b) bifurcation of the West Greenland Current, with one branch  
257 continuing northward along the west coast of Greenland and the other flowing westward across  
258 the Labrador Sea; and (c) the westward flow across the Labrador Sea merging with the  
259 southward Baffin Island Current out of Baffin Bay and southeastward flow out of Hudson Strait  
260 to form the Labrador Current, the equatorward limb of the North Atlantic Subpolar Gyre. This  
261 current has branches along the Labrador coast and the shelf break. Near the Grand Banks, the  
262 Labrador Current meets the poleward Gulf Stream, the poleward limb of the North Atlantic  
263 Subtropical Gyre. Both simulations also reproduce the relatively cold and fresh water over  
264 continental shelves, with especially low values of salinity in Hudson Bay and the St. Lawrence  
265 Estuary. The three major differences between the simulations are that: (a) the bifurcation of the  
266 West Greenland Current has a stronger northward branch in Prog; (b) the Gulf Stream in Prog is  
267 closer to the continental shelf; and (c) the Gulf of St. Lawrence is warmer and saltier in Prog,  
268 both at the surface and in model results interpolated to the 100-m depth. As discussed below,  
269 comparison of model results to observations or reanalysis suggests the results of Ctrl are more  
270 realistic than those from Prog. Seasonal-means of these simulated fields, shown in Appendix B,  
271 indicate that differences between the simulations are more prominent in summer than in winter.

### 272 **3.2 Model performance for currents, temperature, and salinity**

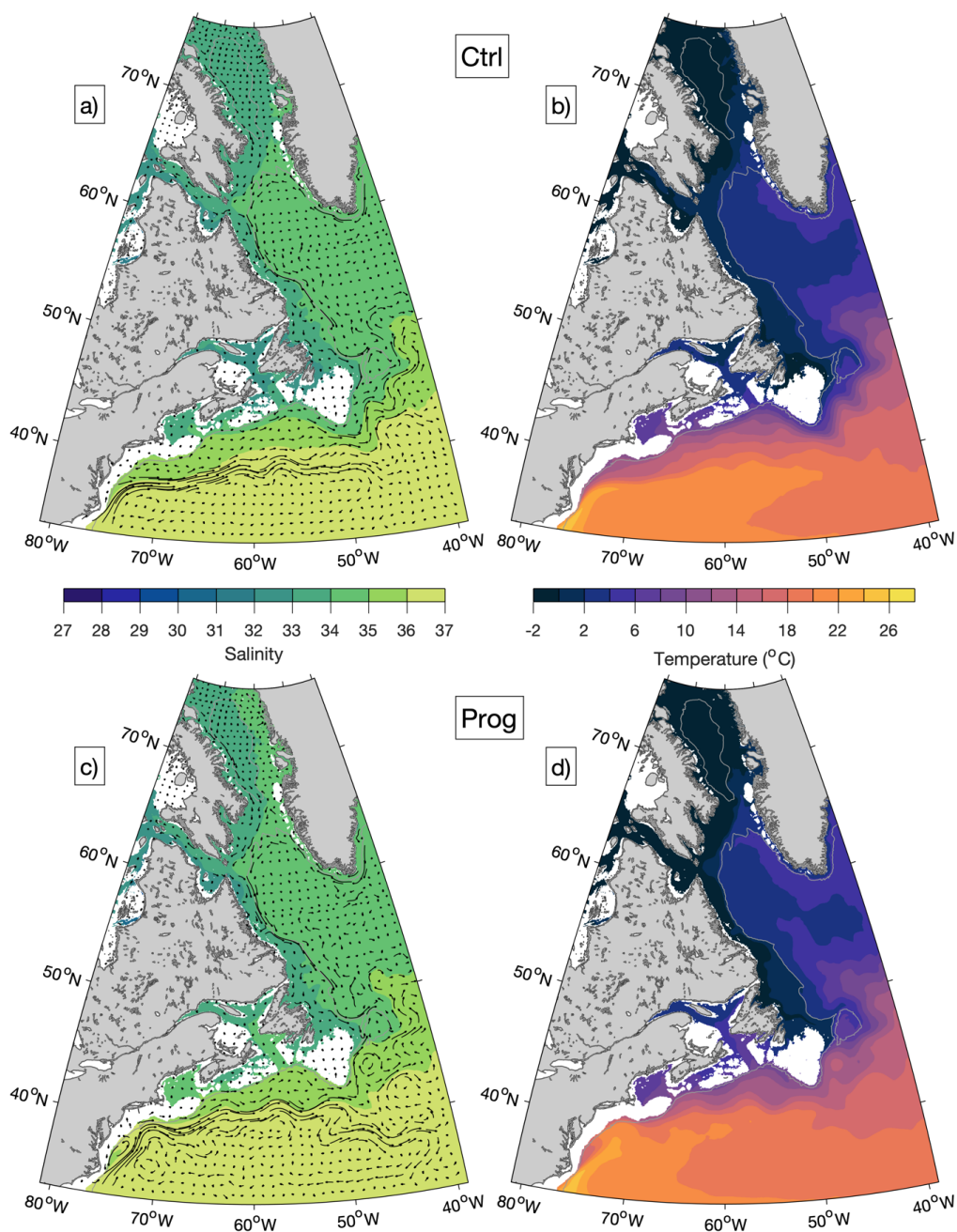
273 To assess the model's performance in simulating currents, temperature, and salinity, we divide  
274 the model domain into nine regions (Fig. 1b) and calculate metrics in each region for model  
275 results at the sea surface and interpolated to the 100-m depth. Within a given region, each model  
276 grid point is weighted by its horizontal area when regional averages are calculated. The areas  
277 along the model's lateral boundaries in which the simulated tracers and currents are nudged  
278 towards GLORYS are not included in the calculations.

279 To quantify model performance for temperature and salinity at the sea surface, root-mean-square  
280 errors (RMSE) of monthly-mean model results are calculated with respect to monthly means of  
281 observations that are linearly interpolated to the model grid. Temperature and salinity at the  
282 surface are compared to 1/4°-grid analysed data sets that combine satellite and in situ  
283 observations: the daily data set OISST (Optimum Interpolation Sea Surface Temperature, v2.0  
284 for 2015–2017 and v2.1 for 2018; Huang et al., 2021) for temperature and the weekly data set  
285 SMOS (Soil Moisture Ocean Salinity; Buongiorno Nardelli et al., 2016) for salinity. For model



286  
287  
288  
289  
290  
291

**Figure 2.** Temporal-mean salinity (a, c) and temperature (b, d) at the sea surface, averaged over 2015–2018, from runs Ctrl (a, b) and Prog (c, d). Also shown in panels (a) and (c) are trajectories representing displacement over five days due to currents at the sea surface averaged over 2015–2018, shown at every 24 model grid points. The gray contour line represents the 1000-m water depth.



292  
293  
294

Figure 3. Similar to Fig. 2 but for model results interpolated to the 100-m depth.



295 results interpolated to the 100-m depth, where gridded observational data sets are not available,  
296 root-mean-square differences (RMSD) of temperature and salinity are calculated with respect to  
297 their respective GLORYS values. It should be noted that GLORYS is based on simulations that  
298 do not include tides (Lellouche et al., 2018), which may affect the accuracy of its temperature  
299 and salinity distributions in addition to that of its currents.

300 The RMSE and RMSD of temperature from the two simulations (Figs. 4–5) are similar over the  
301 northern part of the model domain in that the largest errors tend to occur at the surface in GRS  
302 (Greenland Shelf) throughout the year, and in HST (Hudson Strait) and BB (Baffin Bay) during  
303 the summer. Within these three areas, the largest values of RMSE/RMSD occur in HST at the  
304 surface (about 3.5 °C in Ctrl and 2.9 °C in Prog, both in July). The corresponding biases of  
305 surface temperatures (not shown) indicate a tendency for overestimation (+0.3°C–+2.2°C in  
306 GRS, and -0.4°C–+1.9°C and -0.5°C–+1.0°C during summer in HST and BB respectively for  
307 Prog). Thus, the largest errors occur near the model’s lateral open boundaries, during periods  
308 when sea ice (which would tend to keep the temperature near freezing) is less in HST and BB,  
309 and at the surface where the performance metrics are calculated with respect to an independent  
310 observational data set instead of GLORYS which is also used as lateral boundary input. This  
311 suggests GLORYS as a possible source of model errors, although a detailed examination is  
312 beyond the scope of this study. The slightly larger RMSE of the simulated surface temperature in  
313 Ctrl than in Prog over these areas may be related to the larger underestimation of sea ice in Ctrl,  
314 which will be discussed in Sect. 3.3.

315 Further south, in SPG (Subpolar Gyre), the RMSE/RMSD are smaller in Ctrl than in Prog. The  
316 RMSE at the surface has the range 0.6–1.6 in Ctrl and 0.9–2.1 in Prog, and the RMSD for model  
317 results interpolated to the 100-m depth has the range 0.7–1.4 in Ctrl and 0.9–2.0 in Prog. This  
318 suggests the West Greenland Current simulated in Ctrl, in which the branch of the current that  
319 separates from the Greenland coast dominates, and its associated temperature distribution are  
320 more realistic. The RMSE/RMSD in LS (Labrador Shelf) are similar between the simulations,  
321 ranging from 0.4 to 1.9 in Ctrl and 0.4 to 1.4 in Prog.

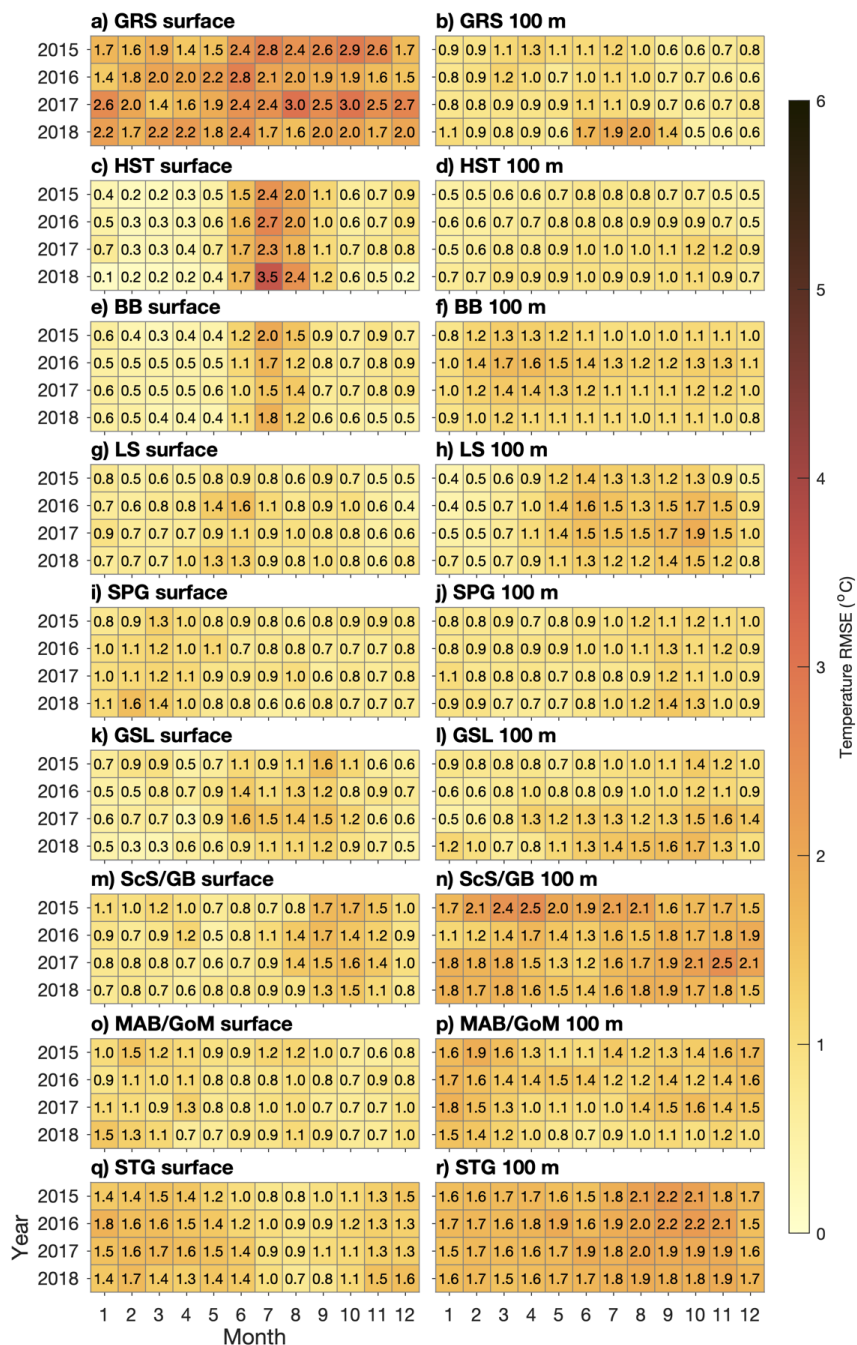
322 The results of Ctrl clearly outperform those of Prog over the southern part of the model domain,  
323 with a maximum RMSE/RMSD of ~2.5°C in the former and ~5.2°C in the latter, both occurring



324 in ScS/GB (Scotian Shelf/Grand Banks) for model results interpolated to the 100-m depth. This  
325 indicates the Gulf Stream simulated in Ctrl, flowing further from the coast than in Prog (Figs. 2–  
326 3), is more realistic. In addition to STG (Subtropical Gyre) where the Gulf Stream itself flows,  
327 the RMSE/RMSD in Ctrl are smaller both at the surface and the 100-m depth in ScS/GB,  
328 MAB/GoM (Mid-Atlantic Bight/Gulf of Maine), and GSL (Gulf of St. Lawrence), all of which  
329 are influenced by the warm and salty slope water of which the Gulf Stream water is one  
330 component (Gatien, 1976). The influence of the slope water extending into the GSL at the 100-m  
331 depth (which can also be seen in Fig. 3) is consistent with the observed (e.g., Richaud et al.,  
332 2016) intrusion of slope water into the Gulf of St. Lawrence along the Laurentian Channel.

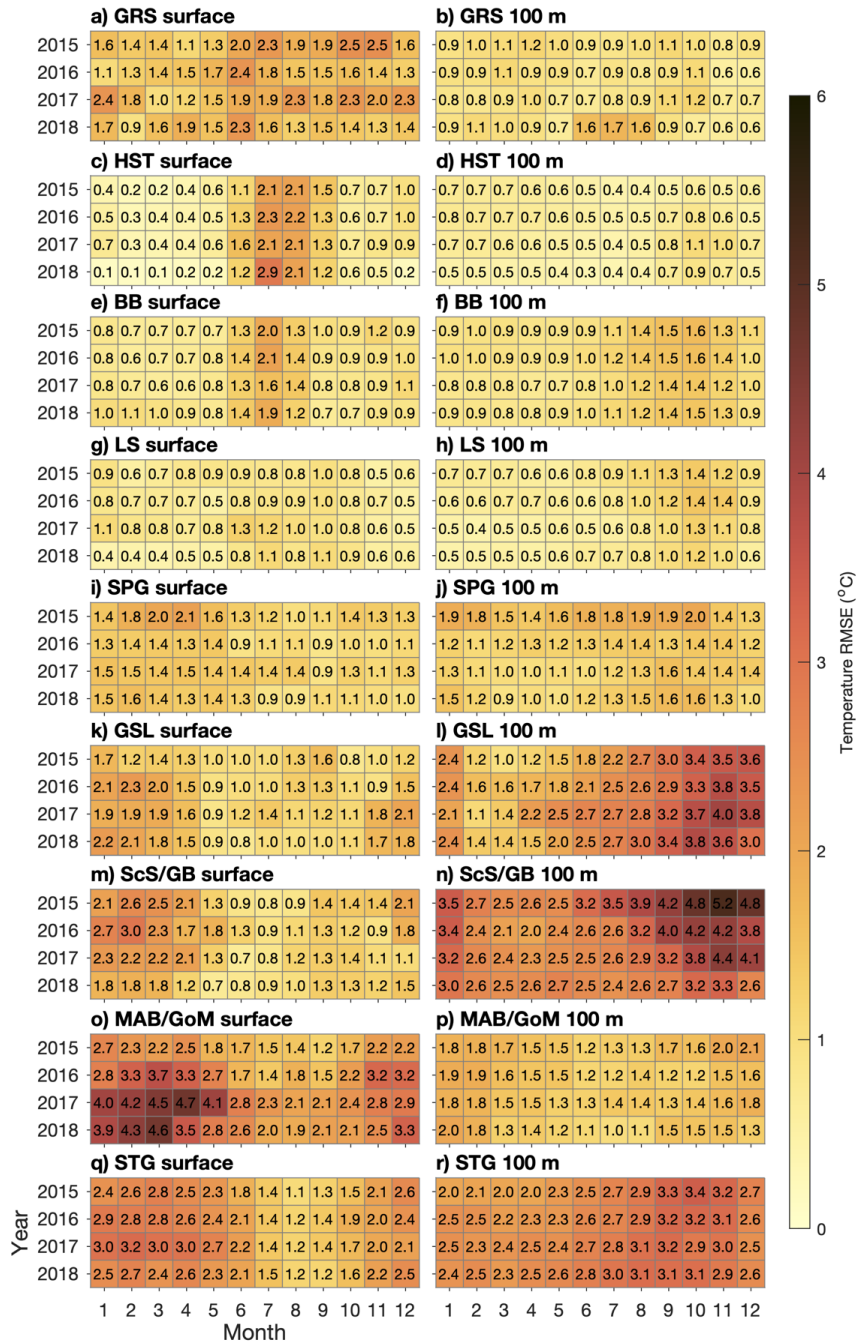
333 The RMSE and RMSD of salinity for both simulations (Figs. 6–7) in the northern part of the  
334 domain are similar to those of temperature in that they tend to be largest at the surface in  
335 summer, especially in HST where the RMSE has maximum values of  $\sim 2.7$  in Ctrl and  $\sim 3.7$  in  
336 Prog. In contrast to the temperature metrics, the surface salinity metrics in GRS undergo an  
337 annual cycle similar to those in HST and BB, being larger during summer and fall than during  
338 the rest of the year. During the months when the RMSE are largest, the surface salinity biases for  
339 Prog are negative in GRS and BB ( $\sim -1.0$ ) and positive in HST (up to  $\sim +1.5$ ). In SPG and LS the  
340 RMSE/RMSD are generally smaller in Ctrl than in Prog (0.1–0.8 for Ctrl and 0.4–1.5 in Prog for  
341 the two regions combined), which is consistent with the metrics for temperatures discussed  
342 above.

343 In the southern part of the domain, Ctrl has much smaller RMSE than Prog in GSL, ScS/GB, and  
344 MAB/GoM (e.g., the maximum value is  $\sim 1.7$  for Ctrl and  $\sim 3.7$  for Prog in MAB/GoM). The  
345 corresponding biases for Prog in these areas are consistently positive (up to  $\sim +3.3$  in GSL),  
346 indicating overestimation. However, within GSL, the 2015–2018 mean of summer surface  
347 salinity simulated by Prog is lower than its counterpart from Ctrl by up to  $\sim 3.5$  in the St.  
348 Lawrence Estuary, but higher by  $\sim 2$  further downstream in the Gulf of St. Lawrence (not shown).  
349 This suggests the model is not able to fully reproduce the propagation of low-salinity water from  
350 the St. Lawrence Estuary (where the salinity is underestimated) to areas downstream of it (where  
351 the salinity is overestimated).



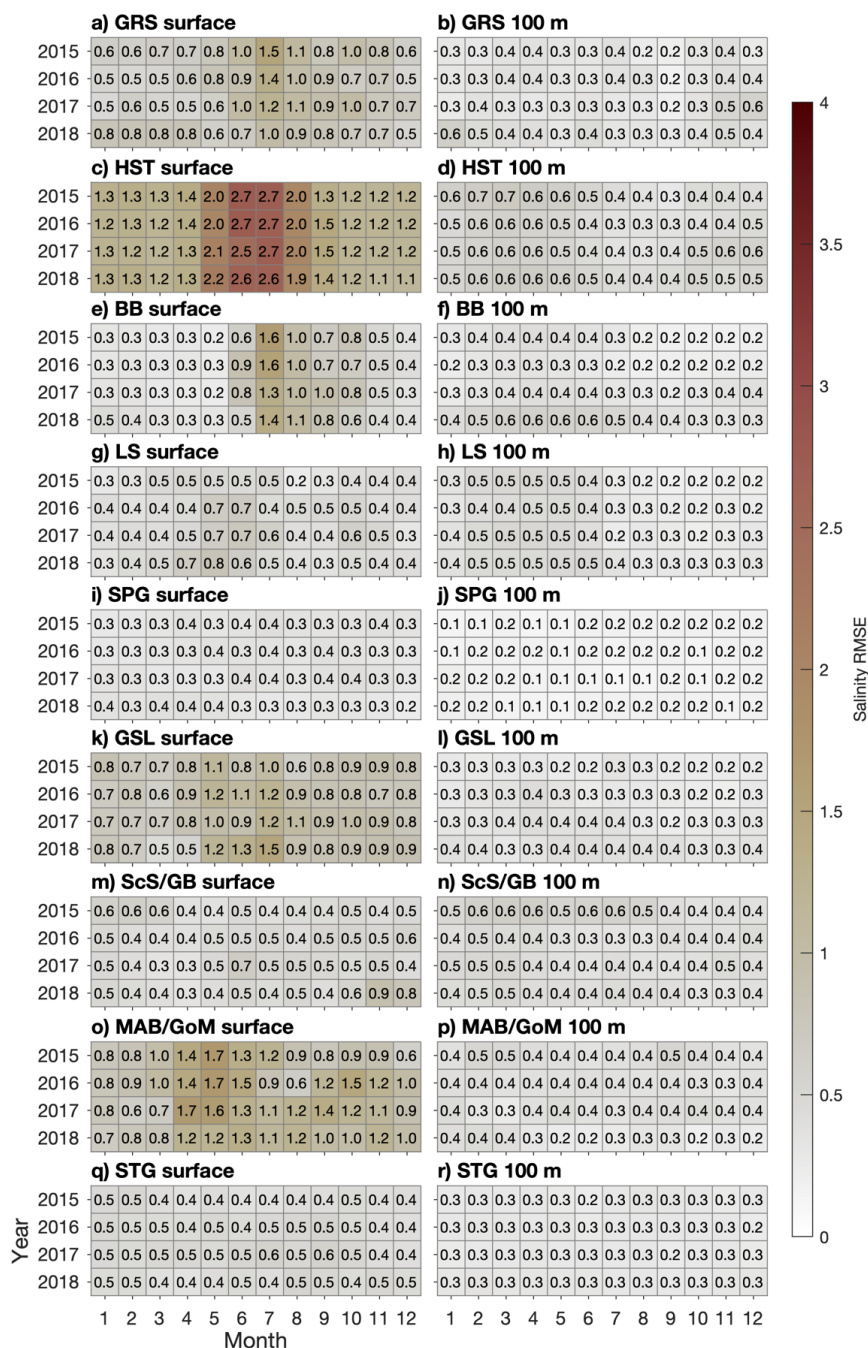
352  
353  
354  
355  
356

**Figure 4.** Root-mean-square-errors/differences of temperatures simulated in Ctrl, calculated for the regions shown in Fig. 1b with respect to the observation-derived OISST data set at the surface and GLORYS reanalysis for model results interpolated to the 100-m depth.



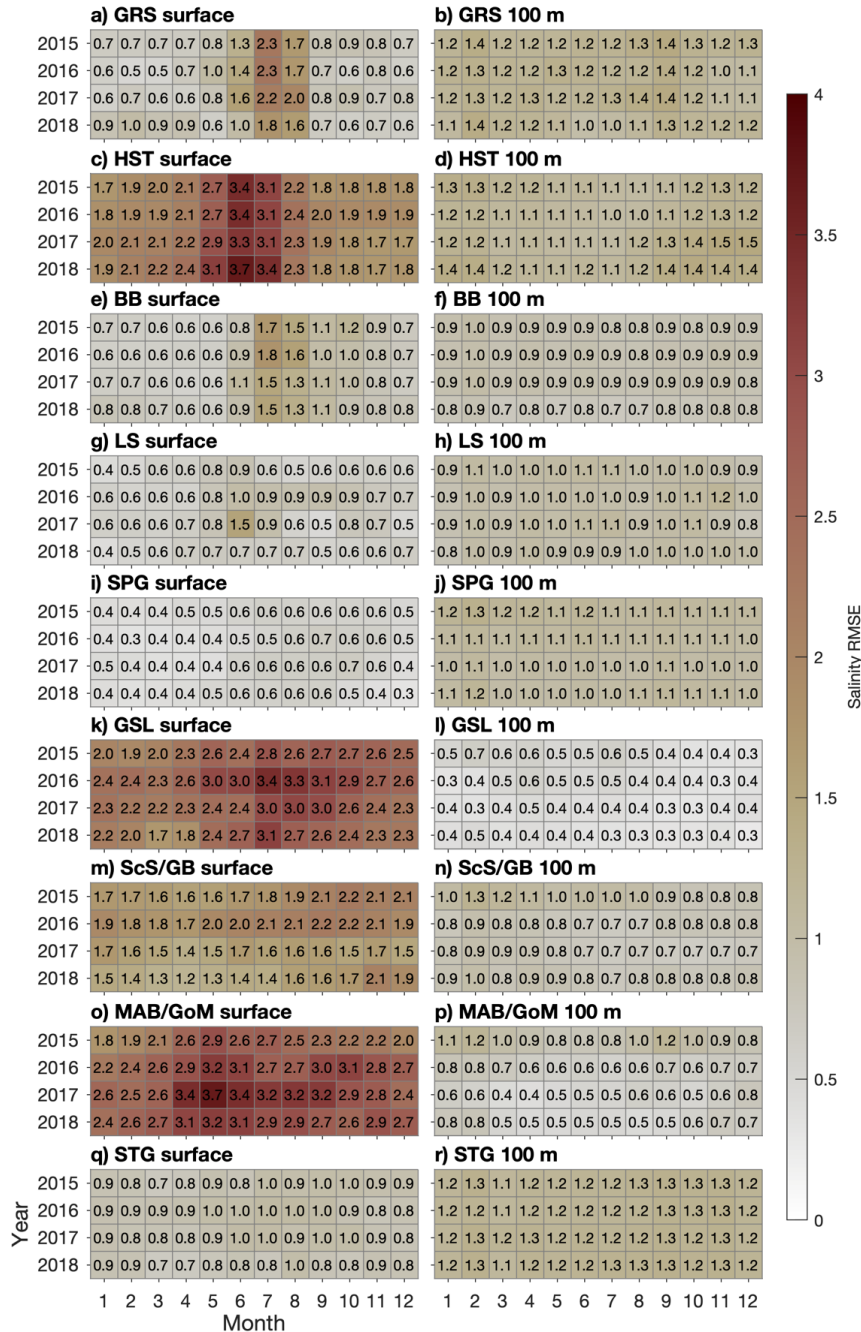
357  
358  
359

Figure 5. Similar to Fig. 4 but for temperatures simulated in Prog.



360  
361  
362  
363  
364

**Figure 6.** Root-mean-square-errors/differences of salinity simulated in Ctrl, calculated for the regions shown in Fig. 1b with respect to the observation-derived SMOS data set at the surface and GLORYS reanalysis for model results interpolated to the 100-m depth.



365  
366  
367  
368

Figure 7. Similar to Figure 6 but for salinity simulated in Prog.



369 A possible cause of this discrepancy between observed and simulated salinity values in the St.  
370 Lawrence Estuary-Gulf system is spurious diapycnal mixing generated by the third-order  
371 upstream advection scheme used for tracers in this study (Marchesiello et al., 2009). We found  
372 that switching to the fourth-order Akima scheme produced salinity and sea ice distributions in the  
373 Gulf that were generally more realistic, but this option was not pursued further because the  
374 scheme is prone to over- or under-shooting, which resulted in patches of unrealistic tracer values  
375 in areas such as the Grand Banks where strong horizontal gradients occur. (This problem has  
376 been reported by Naughten et al. (2017), who simulated the Southern Ocean using ROMS and  
377 CICE). A potential solution is a fourth-order advection scheme in which spurious values are  
378 reduced with a flux limiter, as has been demonstrated by Sheng (2002) for a z-level model.

379 For currents, the model performance is evaluated using a metric known as  $\varepsilon^2$  (Schwab et al.,  
380 1989; Urrego-Blanco and Sheng, 2014):

$$381 \quad \varepsilon^2 = \frac{\sum_{i=1}^N [(u_i^O - \bar{u}_i^O - u_i^M + \bar{u}_i^M)^2 + (v_i^O - \bar{v}_i^O - v_i^M + \bar{v}_i^M)^2]}{\sum_{i=1}^N [(u_i^O - \bar{u}_i^O)^2 + (v_i^O - \bar{v}_i^O)^2]}, \quad (1)$$

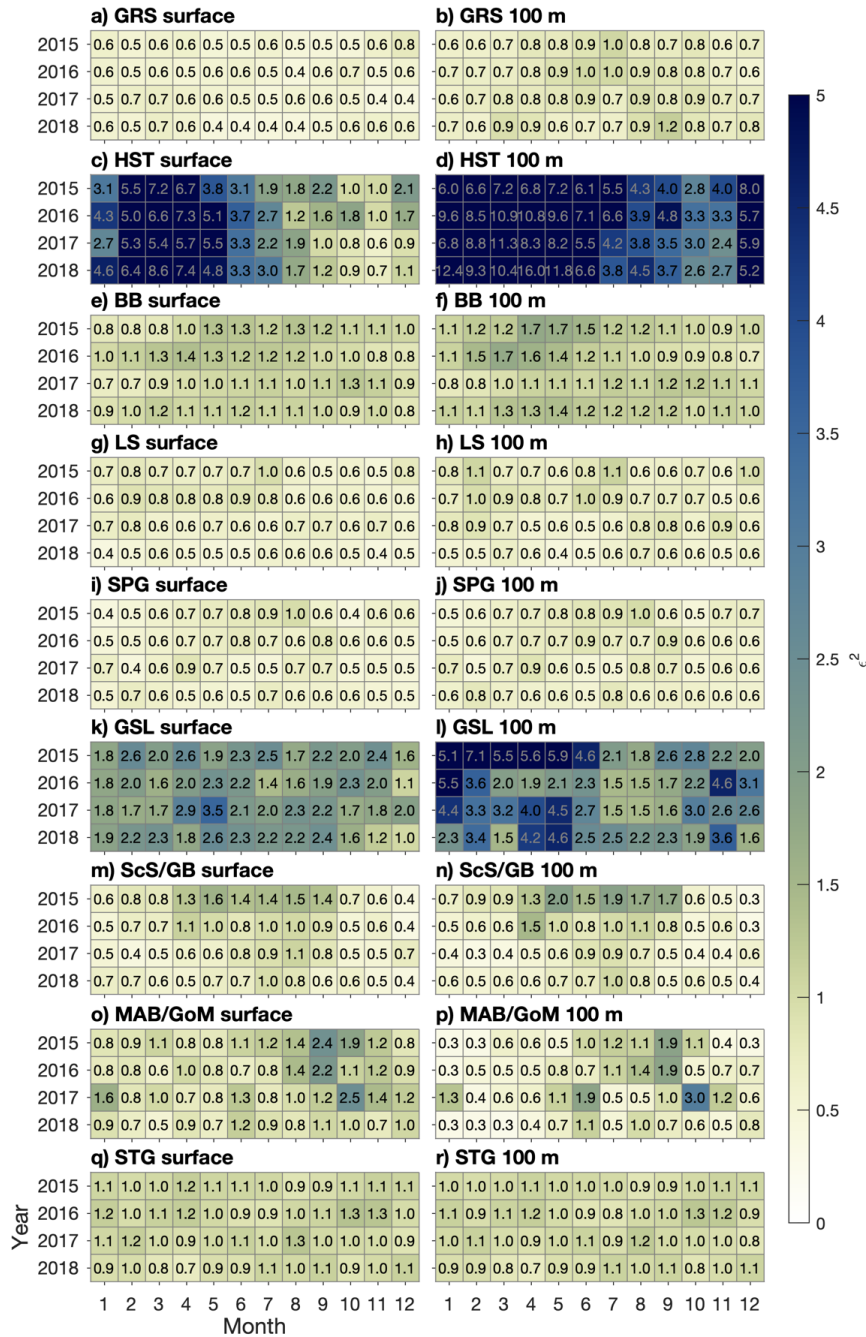
382 where the superscripts  $O$  and  $M$  denote observed and simulated values respectively, overbars  
383 denote spatial averaging over each validation region, and the summation is made over the  
384 validation region. Thus, this metric combines errors for the zonal and meridional current  
385 components and assesses model performance in terms of spatial averages as well as at individual  
386 points, with a value of zero corresponding to perfect agreement between model results and  
387 observations. The metric is calculated with respect to GLORYS both at the surface and for model  
388 results interpolated to the 100-m depth.

389 For both simulations, values of  $\varepsilon^2$  (Figs. 8–9) in the southern part of the model domain are  
390 generally smaller in Ctrl than in Prog (e.g., about 0.7–1.3 for Ctrl vs. 1.0–2.2 for Prog in STG),  
391 consistent with the more realistic simulation of the Gulf Stream due to the nudging of salinity  
392 and temperature in Ctrl. In SPG and LS, values of  $\varepsilon^2$  are similar between the regions and smaller  
393 in Ctrl than in Prog (about 0.4–1.1 in Ctrl and 0.5–1.6 in Prog for the two regions combined).  
394 This suggests the Labrador Current is more realistic in Ctrl than in Prog, which is consistent with  
395 the conclusion drawn from the temperature metrics that the separation of the West Greenland  
396 Current from the Greenland coast is simulated more accurately in Ctrl.



397 The model errors for both runs are largest in HST, mostly due to the southeastward flow along  
398 the south side of Hudson Strait being stronger in the model than in GLORYS (not shown).  
399 Taking as an example the 2015–2018 mean of monthly-mean currents produced by Prog in  
400 September, the southeastward flow is stronger than that in GLORYS by  $\sim 0.25 \text{ m s}^{-1}$  at the surface  
401 and  $\sim 0.15 \text{ m s}^{-1}$  at the 100-m depth. One possible reason for this large discrepancy is that the  
402 model is likely to be unable to accurately simulate the circulation in Hudson Bay, which is the  
403 source of the southeastward flow through Hudson Strait. Circulation in the Bay consists of  
404 several gyres and is sensitive to river discharge (Ridenour et al., 2019). Our model domain  
405 includes only the eastern part of the Bay (Fig. 1a) and, due to a lack of observations, we use  
406 climatological discharge (mostly calculated from observations in the 1960s or 1970s) for all but  
407 one of the ten rivers emptying into the eastern Bay; these factors cast doubt on the model's  
408 ability to realistically simulate the flow within and out of the Bay.

409 It should also be noted that Hudson Strait is characterized by tides of typically 3–6 m in  
410 amplitude (Drinkwater, 1988). While our model includes tidal forcing, GLORYS, as stated  
411 above, does not. This raises questions about how appropriate GLORYS is as a basis of evaluating  
412 simulated currents in this area. Drinkwater (1988) deployed an array of current meters across  
413 Hudson Strait between August and October of 1982. While exact coordinates of this array are not  
414 available, the grid point in our model closest to the southwestern end of the array (station HS1)  
415 can be approximated as ( $69.47^\circ \text{ W}$ ,  $61.15^\circ \text{ N}$ ), with a water depth of 272 m, from Figs. 1–2 of  
416 Drinkwater (1988). The eight-week average of residual current speeds at this location was  
417 observed to be about  $0.29 \text{ m s}^{-1}$  and  $0.12 \text{ m s}^{-1}$  at the 30-m and 100-m depths respectively. The  
418 2015–2018 average of September-mean current speeds simulated by Prog and from GLORYS at  
419 the corresponding model grid point are similar to each other and somewhat less than the  
420 observed value at the 30-m depth (about  $0.24 \text{ m s}^{-1}$  and  $0.23 \text{ m s}^{-1}$  respectively vs.  $0.29 \text{ m s}^{-1}$ ).  
421 However, at the 100-m depth, the simulated mean current speed ( $0.10 \text{ m s}^{-1}$ ) is more similar to  
422 the observation ( $0.12 \text{ m s}^{-1}$ ) than the GLORYS value ( $0.03 \text{ m s}^{-1}$ ). This points to the possibility  
423 that the inclusion of tides in our model may result in a more realistic vertical structure of currents  
424 in areas where both tides and baroclinity play significant roles. The role of tides in the NWA is  
425 explored further in Sect. 4.1.

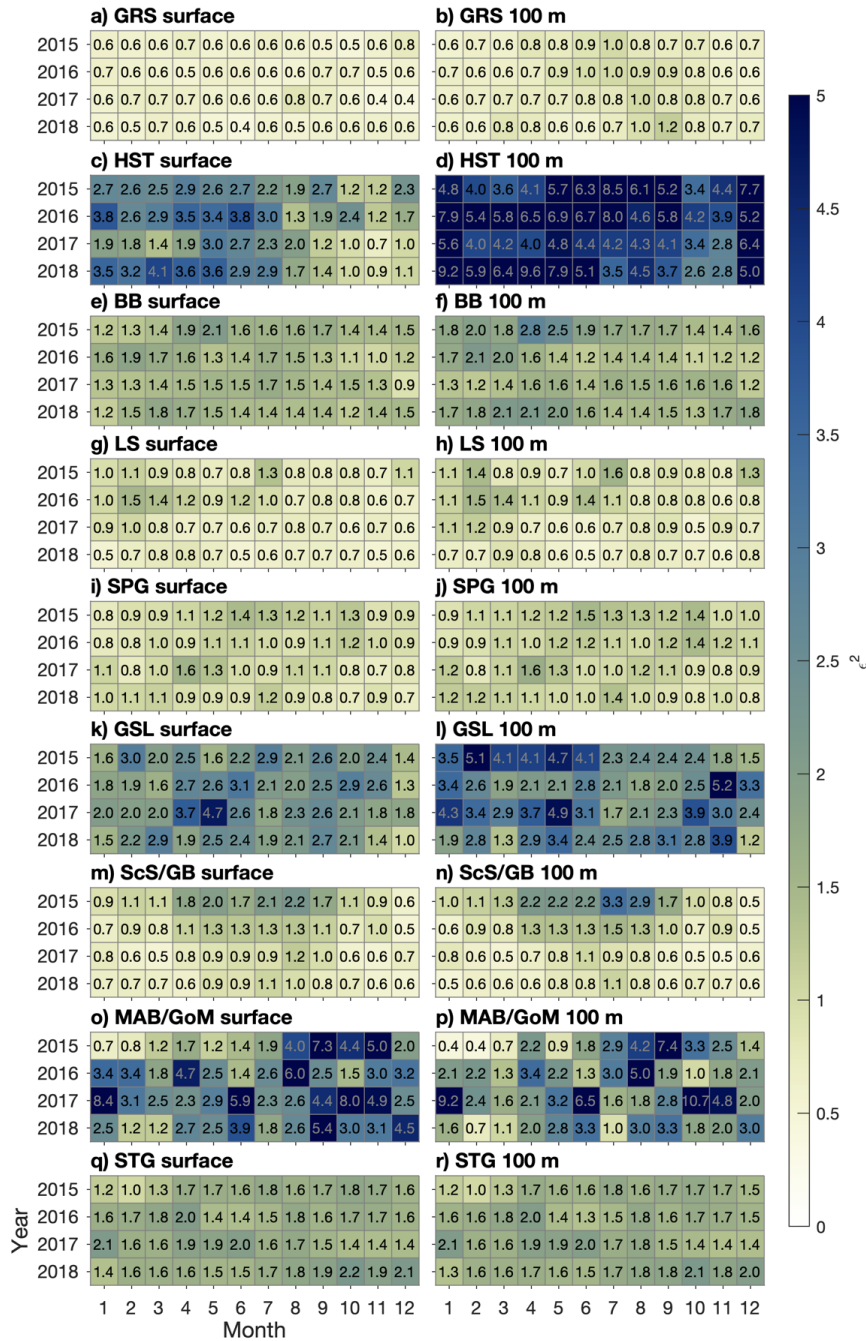


426

427

428 **Figure 8.**  $\epsilon^2$  of currents simulated in Ctrl, calculated for the regions shown in Fig. 1b with respect to GLORYS

429 reanalysis. See Equation 1 for the definition of  $\epsilon^2$ .



430  
431  
432  
433

Figure 9. Similar to Fig. 8 but for currents simulated in Prog.



434 The temperature and salinity simulated in Prog have also been compared to observations made  
435 along transects from the Atlantic Zone Monitoring Program and its off-shelf counterpart (not  
436 shown). RMSE along the AR7W transect, which spans the Labrador Sea between southern  
437 Labrador and southern Greenland, are largest near the surface, reaching  $\sim 2^{\circ}\text{C}$  for temperature  
438 and  $\sim 0.5$  for salinity. The errors are larger in transects across Cabot Strait and across the Scotian  
439 Shelf (up to  $\sim 4^{\circ}\text{C}$  for temperature and  $\sim 3$  for salinity), reflecting the difficulty Prog has in  
440 reproducing the estuarine circulation in the Gulf of St. Lawrence and the positions of the Gulf  
441 Stream and slope waters.

442 The preceding description and evaluation of the simulated circulation and hydrography have  
443 highlighted two features in which the nudging of temperature and salinity in Ctrl leads to  
444 improved model performance: (a) the separation of currents (the Gulf Stream and West  
445 Greenland Current) from their respective coasts and (b) propagation of the low-salinity plume  
446 from the St. Lawrence Estuary. Chassignet and Xu (2017) and Pennelly and Myers (2020)  
447 showed respectively that increasing the horizontal resolution of their model grids from  $1/12^{\circ}$  to  
448  $1/50^{\circ}$  or  $1/60^{\circ}$  resulted in more realistic representations of the Gulf Stream or the West Greenland  
449 Current. Given the computational costs of making coupled physical-biogeochemical simulations  
450 with a finer horizontal grid than what we currently use, a possible way to improve our modelling  
451 system's performance in prognostic simulations would be to nest a finer-resolution grid covering  
452 an area of particular interest (e.g., the Labrador Sea) within the existing  $1/12^{\circ}$  grid. As discussed  
453 earlier, a fourth-order horizontal advection scheme with a flux limiter is a possible way to  
454 improve our model's simulation of estuarine plumes in prognostic simulations.

### 455 3.3 Sea ice

456 February-mean values of sea ice cover and effective sea ice thickness (sea ice cover multiplied  
457 by thickness), averaged over 2015–2018, are shown in Fig. 10. Model results from Ctrl and Prog  
458 are similar in that the ice cover spans Hudson Strait and adjoining areas to its west as well as  
459 most of Baffin Bay, and the thickest ice (thickness  $> \sim 3$  m) occurs along the coasts of those areas.  
460 The two runs are different in that Ctrl produces more ice along the west coast of Greenland and  
461 in the northwest Gulf of St. Lawrence, while Prog produces more ice along the north side of  
462 Hudson Strait and on the Labrador Shelf. The larger sea ice production by Ctrl for the west coast  
463 of Greenland and the northwest GSL is consistent with the lower sea-surface salinity and



464 temperature in this simulation due to the nudging (Fig. 2). For northern Hudson Strait and the  
465 Labrador Shelf, a possible factor in the larger sea ice production by Prog is the fact that, in these  
466 areas, offshore winds tend to cause ice divergence, which in turn leads to new ice formation  
467 (Babb et al., 2021; Prinsenber and Peterson, 1992). The cycle of open water formation,  
468 freezing, and ice divergence implies changes in the surface temperature and salinity over  
469 relatively small spatiotemporal scales, which could be dampened by the nudging of Ctrl to the  
470 monthly CORA data set which has a horizontal resolution of  $0.2^{\circ}$ – $0.5^{\circ}$  in our study area  
471 (Szekely, 2023). The role of sea ice on the physical oceanography of our study area is studied  
472 further in Sect. 4.2.

473 The ice model's performance is evaluated in terms of RMSE with respect to daily AMSR2  
474 (Advanced Microwave Satellite Radiometer) observations, available on a 6.5-km grid  
475 (Melsheimer and Spreen, 2019). The model errors in HST, BB, and LS are generally larger in  
476 Ctrl (Fig. 11) than in Prog (Fig. 12), consistent with the smaller sea ice production in these areas  
477 by the former. In HST, the increase in model error during May for both runs is mostly due to  
478 underestimation, indicating a too-early melting of the ice. Given that this seasonal increase in  
479 model error occurs in both runs, the cause of the underestimation may be related to ice advection  
480 instead of thermodynamics. Examination of sea ice budgets for areas within the NWA is a  
481 possible topic of future studies.

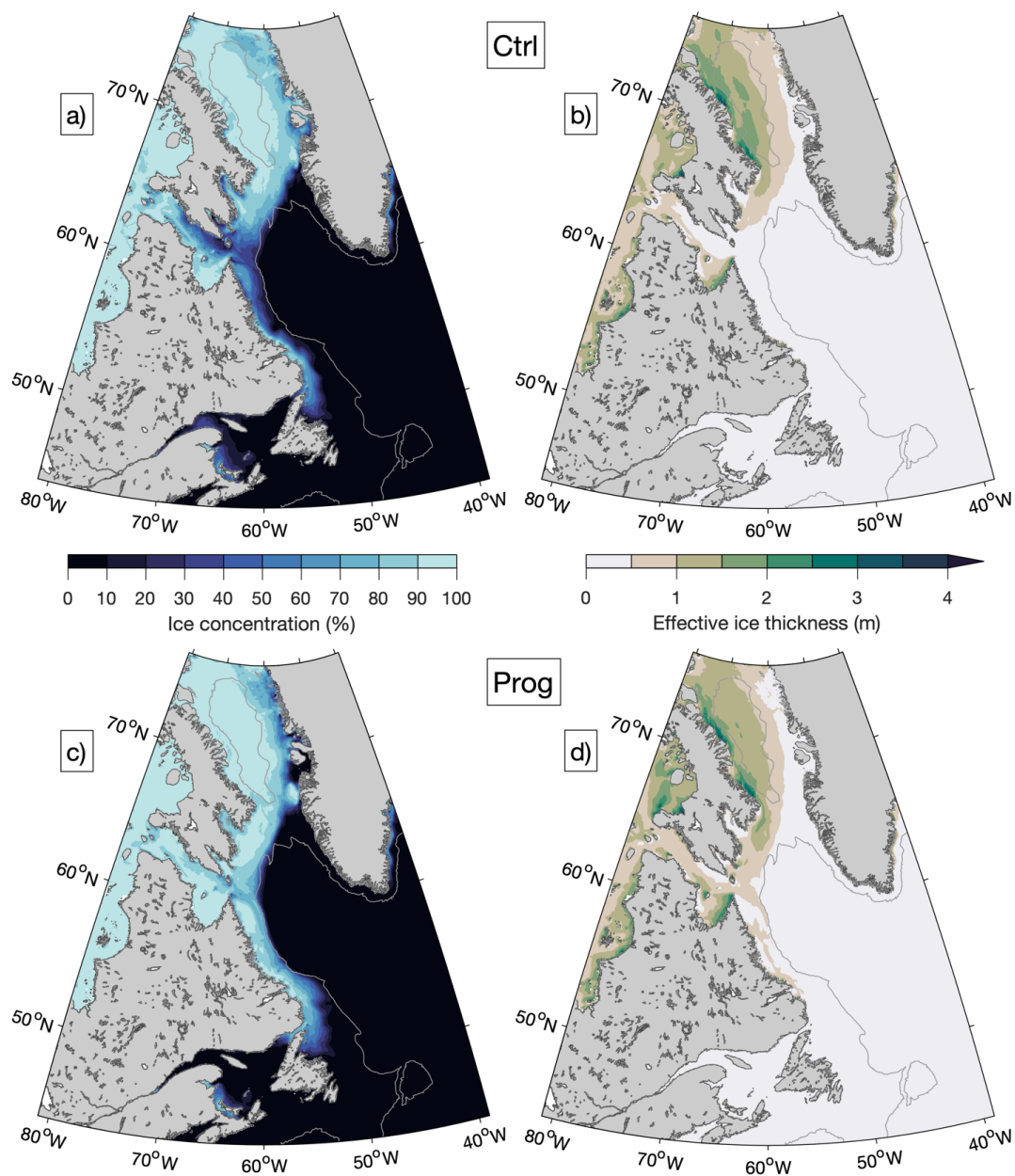
### 482 **3.4 Biogeochemistry**

483 Snapshots of surface nitrate and subsurface oxygen in the Labrador Sea and surrounding areas at  
484 the time of the Atlantic Zone Off-Shelf Monitoring Program (AZOMP) cruise in May 2015 are  
485 shown in Fig. 13. The simulation indicates that nitrate starts to be depleted in the northern  
486 Labrador Sea and along the Labrador shelf at this time but remains high in the deep central  
487 Labrador Sea. Surface and shelf waters are well oxygenated and subsurface conditions along the  
488 AR7W transect are characteristic of the water masses: oxygenated Labrador Sea Water  
489 (depth < 2000 m), lower-oxygen Northeast Atlantic Deep Water (2000–3000 m), and the more  
490 oxygenated Denmark Strait Overflow Water (> 3000 m), which is in line with the observations  
491 along the AR7W transect (Fig. 14a). Simulated nitrate is also characteristic of the three water  
492 masses (Fig. 14b). As also shown in Fig. 13, surface nitrate remains high in the central Labrador



493 Sea but is low or depleted on the West Greenland and Labrador Shelves, respectively. These  
494 patterns agree with the observations. The spatial variability in alkalinity (Fig. 14c) and total

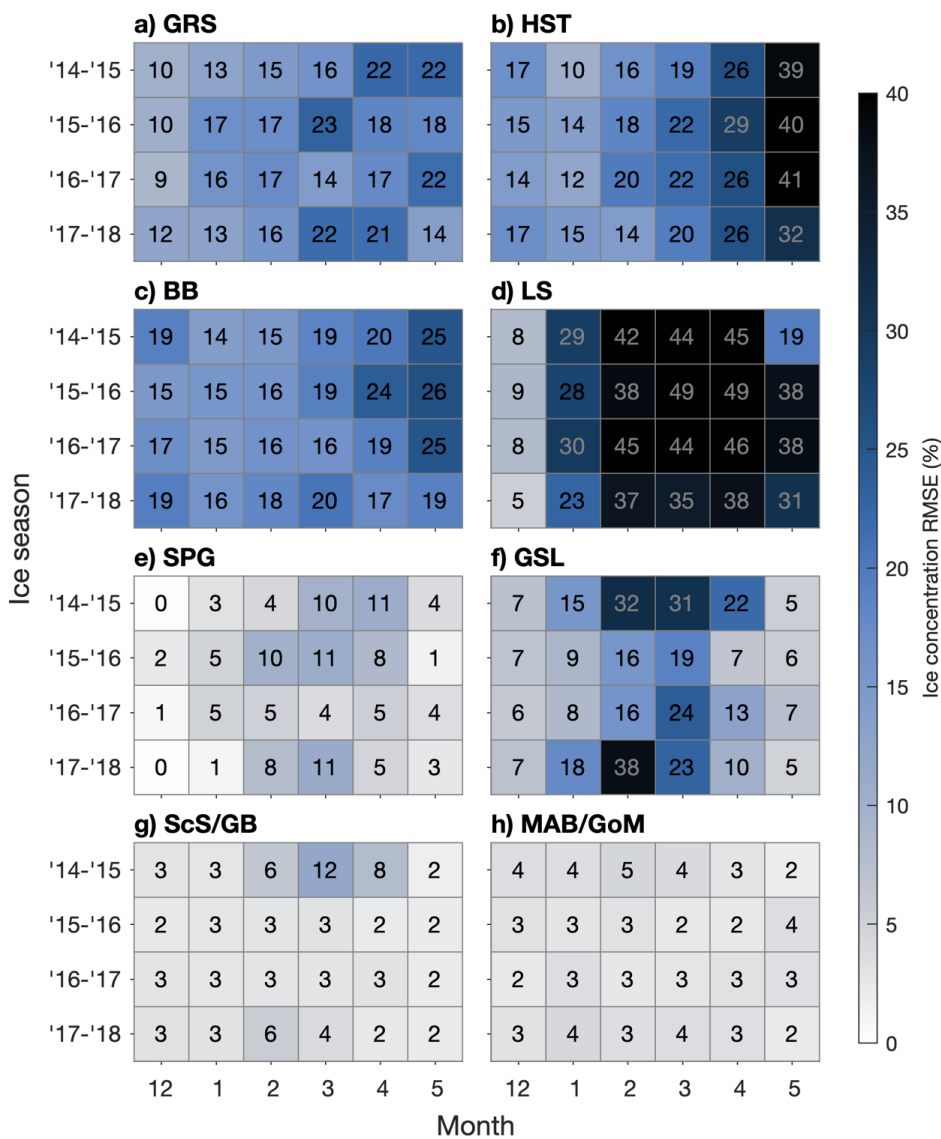
495



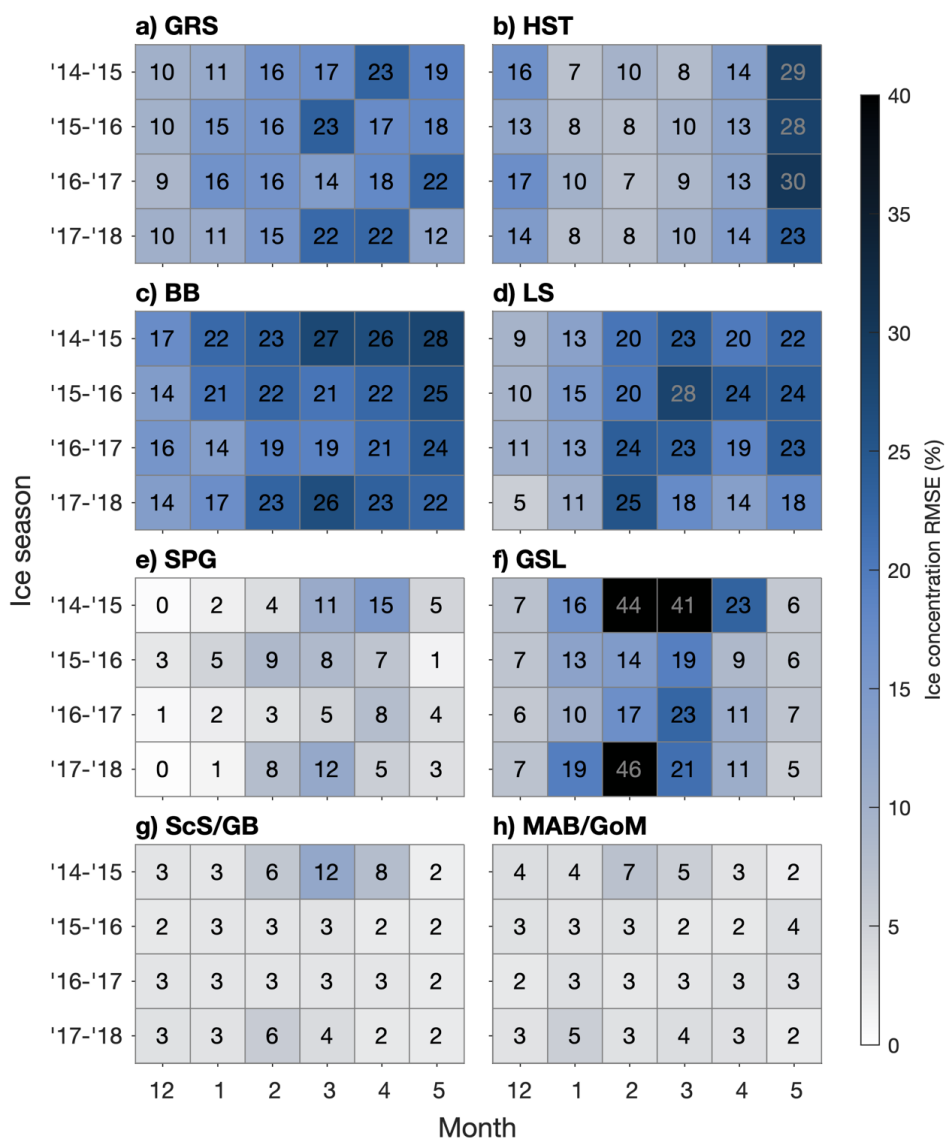
496  
497



498 **Figure 10.** Monthly-mean simulated sea ice concentration (a, c) and effective sea ice thickness (sea ice cover  
 499 multiplied by thickness) (b, d) for February, averaged over 2015–2018, from Ctrl (a, b) and Prog (c, d). The gray  
 500 contour line represents the 1000-m water depth.

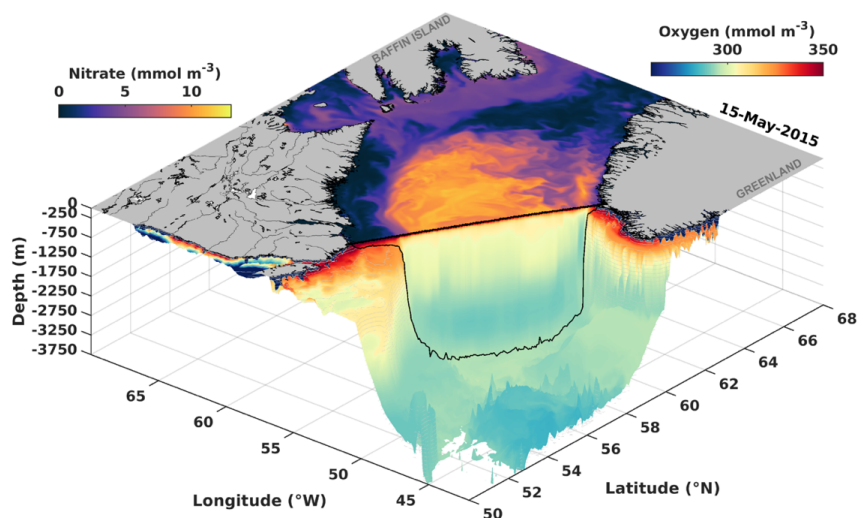


501  
 502  
 503 **Figure 11.** Root-mean-square-errors of ice concentration simulated in Ctrl, calculated for the regions shown in Fig.  
 504 1b with respect to AMSR2 satellite observations.



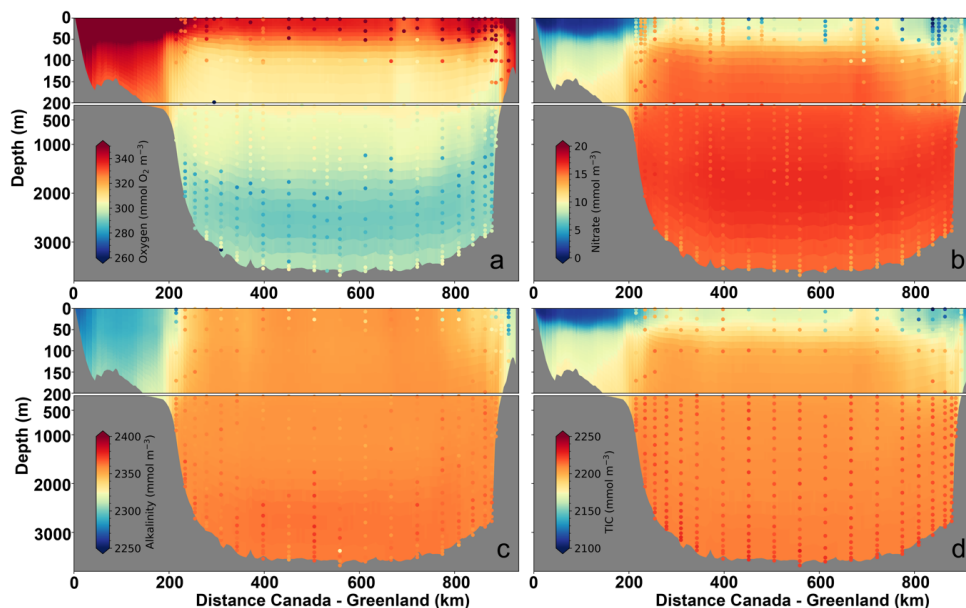
505  
506  
507  
508  
509

Figure 12. Similar to Fig. 11 but for ice concentration simulated in Prog.



510  
511  
512  
513  
514  
515

**Figure 13.** Three-dimensional view of simulated surface nitrate and subsurface oxygen for May 15, 2015. The black dots at the surface correspond to the AR7W transect stations and the black line indicates the location of the bottom for the transect.

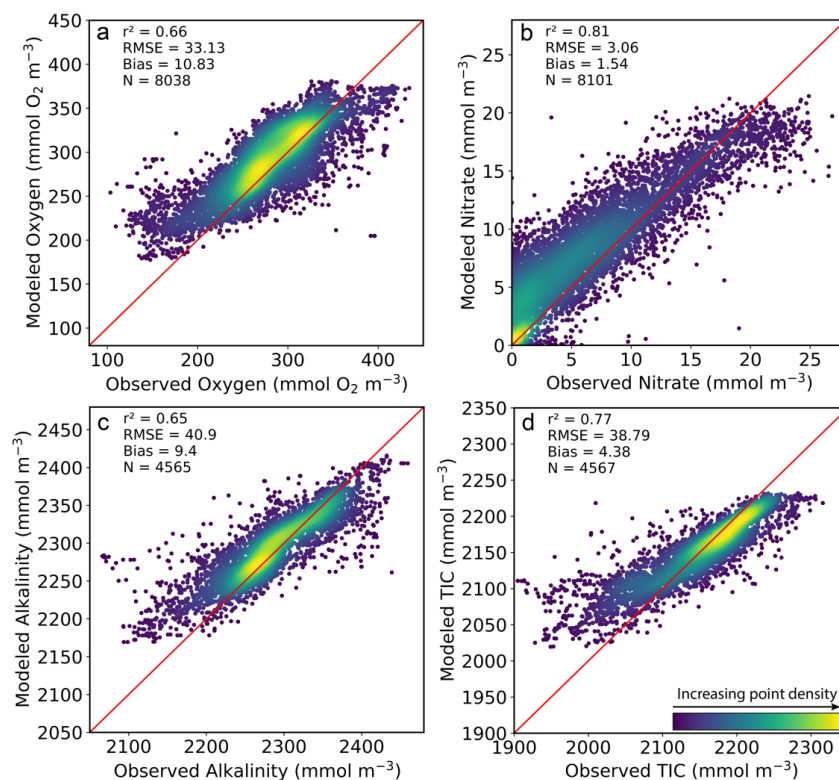


516  
517  
518  
519  
520

**Figure 14.** Comparison of simulated (background) versus observed (dots) for: oxygen (a), nitrate (b), alkalinity (c), and total inorganic carbon (d) during the AR7W transect in May 2015. Note: the y-axis has higher resolution in the upper 200 m.



521



522

523

524 **Figure 15.** Comparison between simulated values and AZMP/AZOMP bottle observations during 2014–2018 for:

525 oxygen (a), nitrate (b), alkalinity (c), and total inorganic carbon (d). N is the number of observations used for the

526 comparison.

527

528 inorganic carbon (TIC; Figure 14d) along the AR7W transect is also well represented. The largest

529 mismatch occurs for TIC which is underestimated in the subsurface layers (depths > 200 m).

530 Comparison of simulated oxygen, nitrate, alkalinity, and TIC to AZMP/AZOMP in situ

531 observations, at locations ranging from the Gulf of Maine to the Labrador Shelf, was carried out

532 for the period 2014–2018 (Fig. 15). The model simulates reasonably well the spatial and

533 temporal variability in biogeochemical variables ( $0.65 < r^2 < 0.81$ ). Simulated oxygen has a small

534 positive bias (10.8 mmol m<sup>-3</sup>, Fig. 15a) but otherwise agrees with observations. Nitrate has the

535 best match with observations ( $r^2 = 0.81$ ) but with a small positive bias (Fig. 15b), possibly driven



536 by excess vertical mixing or by a delay in the seasonal uptake. The small bias at low TIC (i.e.,  
537 surface) is likely to have the same source (Fig. 15d).

#### 538 **4 Sensitivity studies**

539 The ocean circulation and sea ice modules of DalROMS-NWA12 v1.0 are used in this section to  
540 examine the roles of tides and sea ice in the hydrodynamics of the NWA. This is done by  
541 comparing the model results from Prog to those from two additional simulations that are  
542 identical to Prog but with the tidal forcing absent from one (NoTides) and sea ice absent from the  
543 other (NoIce). In NoIce, the net surface heat flux is set to zero if it would cool the ocean and the  
544 sea surface temperature is already at or below the local freezing temperature. The difference  
545 between surface temperatures simulated in Prog and in NoTides (Prog minus NoTides) will be  
546 denoted  $\Delta T_{sfc}^{P-NT}$  and the difference in bottom temperatures will be denoted  $\Delta T_{btm}^{P-NT}$ . Similar  
547 notations will be used for differences in salinity (e.g.,  $\Delta S_{sfc}^{P-NT}$ ) and current speed (e.g.,  
548  $\Delta |\vec{V}|_{sfc}^{P-NT}$ ) and for differences between model results from Prog and NoIce (e.g.,  $\Delta T_{sfc}^{P-NI}$ ).

#### 549 **4.1 The effect of tides**

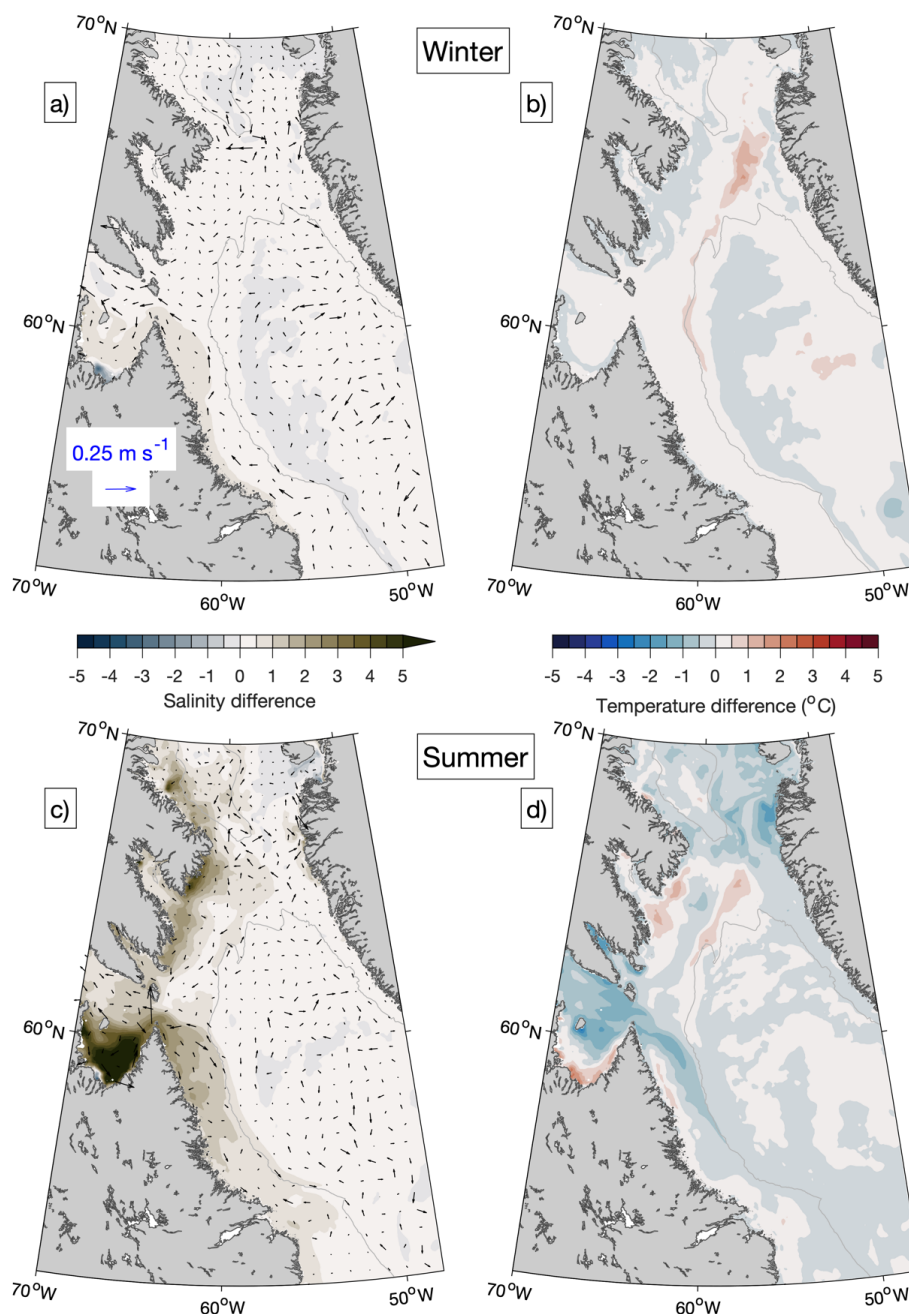
550 Differences between Prog and NoTides (Prog minus NoTides) in sea surface salinity, currents,  
551 and temperature over Baffin Bay and the Labrador Sea, averaged over the winters (December–  
552 February) and summers (June–August) of December 2014–August 2018, are shown in Fig. 16. In  
553 winter (Fig. 16a–b), differences between the simulations of temperature and salinity over this  
554 area are relatively small – generally within  $\pm 1$  for salinity, and up to  $\sim +1.5^\circ\text{C}$  for temperature. In  
555 summer (Fig. 16c–d),  $\Delta S_{sfc}^{P-NT}$  is positive along most of the Baffin Island coast, in Ungava Bay,  
556 and on the northern Labrador Shelf (up to  $\sim 7$  in Ungava Bay) while  $\Delta T_{sfc}^{P-NT}$  is mostly negative  
557 throughout the area but especially over shelves ( $\sim -1^\circ\text{C}$ ). These differences between Prog and  
558 NoTides are consistent with the presence of sea ice over large portions of this area during winter,  
559 given that sea ice can modulate tidal mixing and thus tend to reduce the differences between the  
560 ocean states simulated with and without tides. In summer, the presence of tidal mixing in Prog  
561 contributes to vertical mixing over shelf areas, resulting in surface waters that are saltier and  
562 colder than if there were no tides and the water column were more highly stratified. There are,  
563 however, areas in which the inclusion of tides results in positive  $\Delta T_{sfc}^{P-NT}$  during the summer,



564 notably along the coast of Ungava Bay. Given that  $\Delta S_{sfc}^{P-NT}$  is positive throughout the Bay, the  
565 contrast between positive  $\Delta T_{sfc}^{P-NT}$  along the coast and negative  $\Delta T_{sfc}^{P-NT}$  near the Bay's mouth  
566 suggests air-sea fluxes might differ between the two parts of the Bay.

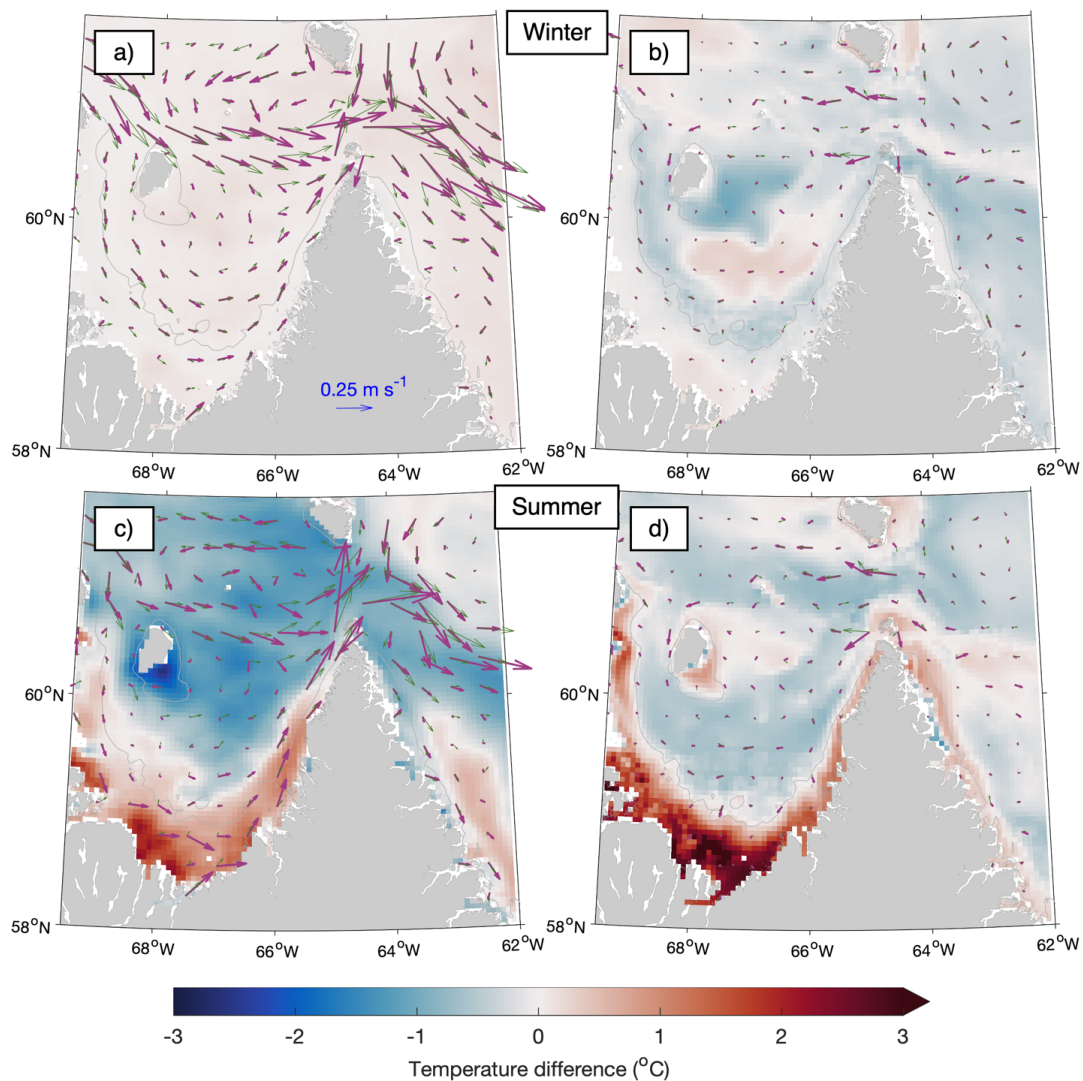
567 The effect of tides on water temperature within Ungava Bay is explored in Figs. 17 and 18. In  
568 winter, the models results from Prog and NoTides are similar not only in terms of the surface  
569 temperature (Fig. 17a), but also in terms of bottom temperature ( $|\Delta T_{btm}^{P-NT}| < \sim 1^\circ\text{C}$ , Fig. 17b) and  
570 current speeds at both the surface and bottom ( $\Delta|\vec{V}|_{sfc}^{P-NT}$  and  $\Delta|\vec{V}|_{btm}^{P-NT} < \sim 0.1 \text{ m s}^{-1}$ , Fig. 17a–b).  
571 In summer at the sea surface (Fig. 17c), both  $\Delta|\vec{V}|_{sfc}^{P-NT}$  and  $\Delta T_{sfc}^{P-NT}$  are positive along the coast  
572 but generally negative in the outer bay. Along the bottom in summer (Fig. 17d),  $\Delta T_{btm}^{P-NT}$  is  
573 positive and as large as  $\sim +4^\circ\text{C}$  along the coast, while in the outer bay  $\Delta T_{btm}^{P-NT}$  is small  
574 ( $|\Delta T_{btm}^{P-NT}| < \sim 1^\circ\text{C}$ ) and the currents are generally weak in both simulations. The patterns of mean  
575 summer sea ice concentration are also different between the two simulations, with the ice cover  
576 produced in Prog (Fig. 18a) being highest over the outer bay (up to  $\sim 40\%$ ) and low near the  
577 coast, while NoTides (Fig. 18b) produces a wide area of high ice cover along the coast (up to  
578  $\sim 90\%$ ). The patterns of mean summer sea surface temperature from the two simulations (Fig.  
579 18c–d) correspond to those of the sea ice cover, with areas of higher (lower) ice cover  
580 corresponding to lower (higher) temperatures. Given that the only difference between the Prog  
581 and NoTides simulations is the inclusion of tides in the former, these results suggest that tides  
582 along the coast of Ungava Bay promotes an earlier disappearance of ice there during the summer,  
583 and this in turn leads to a larger flux of solar radiation into the ocean and a less impeded flow.

584 The effect of tides is also evident in the region surrounding two other areas with large tidal  
585 ranges, the St. Lawrence Estuary and the Bay of Fundy. In both winter and summer,  $\Delta S_{sfc}^{P-NT}$  in  
586 the St. Lawrence Estuary (Fig. 19a,c) is positive (up to  $\sim 6$ ), suggesting that tidal mixing brings  
587 higher-salinity subsurface water towards the surface. In summer (Fig. 19c), the influence of this  
588 higher salinity due to tidal mixing spreads into the northwest Gulf of St. Lawrence due to the  
589 propagation of the estuarine plume. The role of tidal mixing is also evident in the patterns of sea  
590 surface temperatures (Fig. 19b,d), with  $\Delta T_{sfc}^{P-NT}$  positive in winter and negative in summer.  
591 Differences between the simulations are also visible over the open ocean for all three fields. As



592  
593  
594  
595  
596  
597

Figure 16. Differences in seasonal-mean simulated sea surface salinity and currents (a, c) and temperature (b, d) over Baffin Bay and the Labrador Sea when model results from NoTides are subtracted from those from Prog, averaged over winters (a, b) and summers (c, d) of 2015–2018. Difference vectors are shown at every 12th model grid point. The gray contour line represents the 1000-m water depth.



598

599

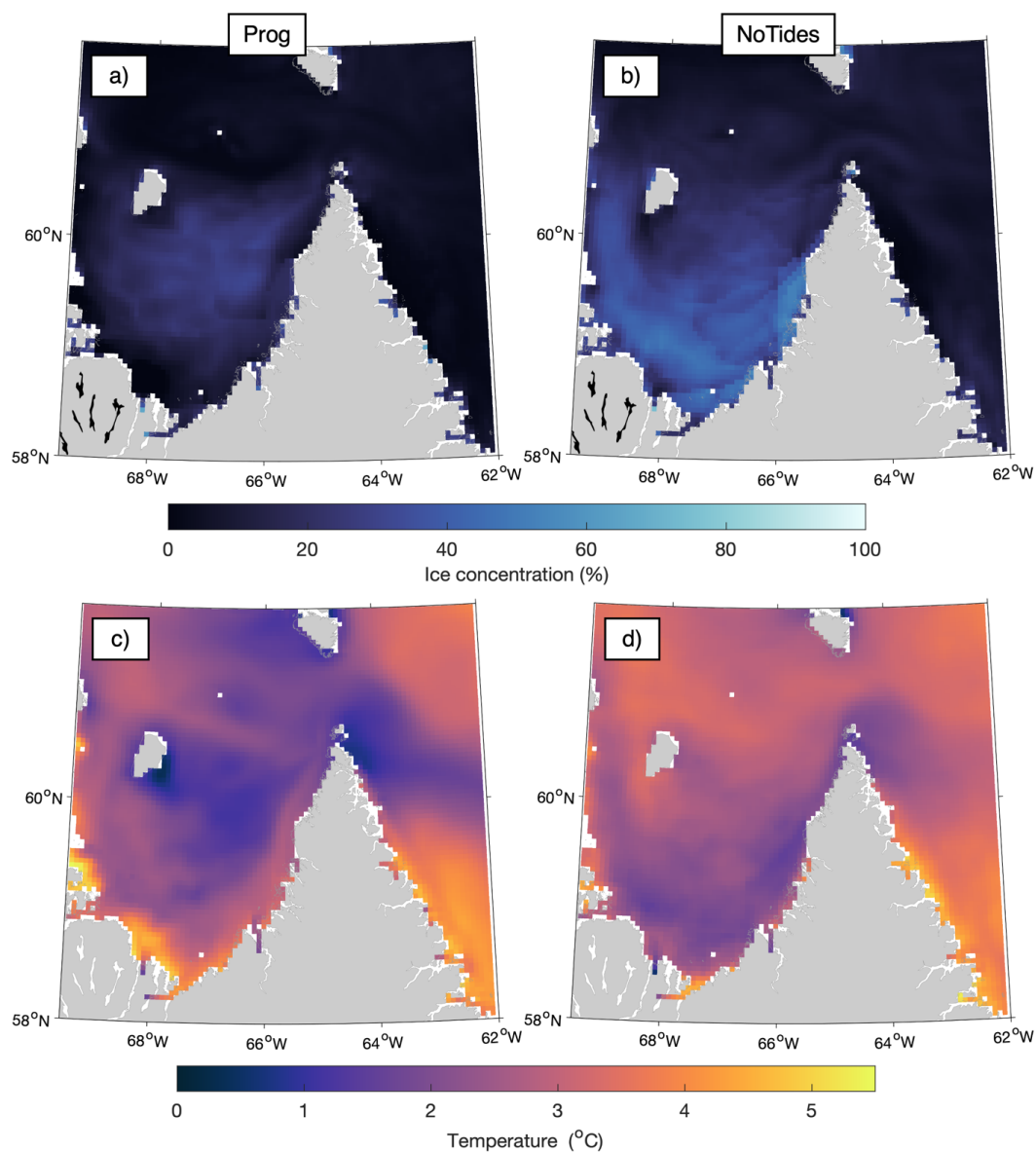
600

601

602

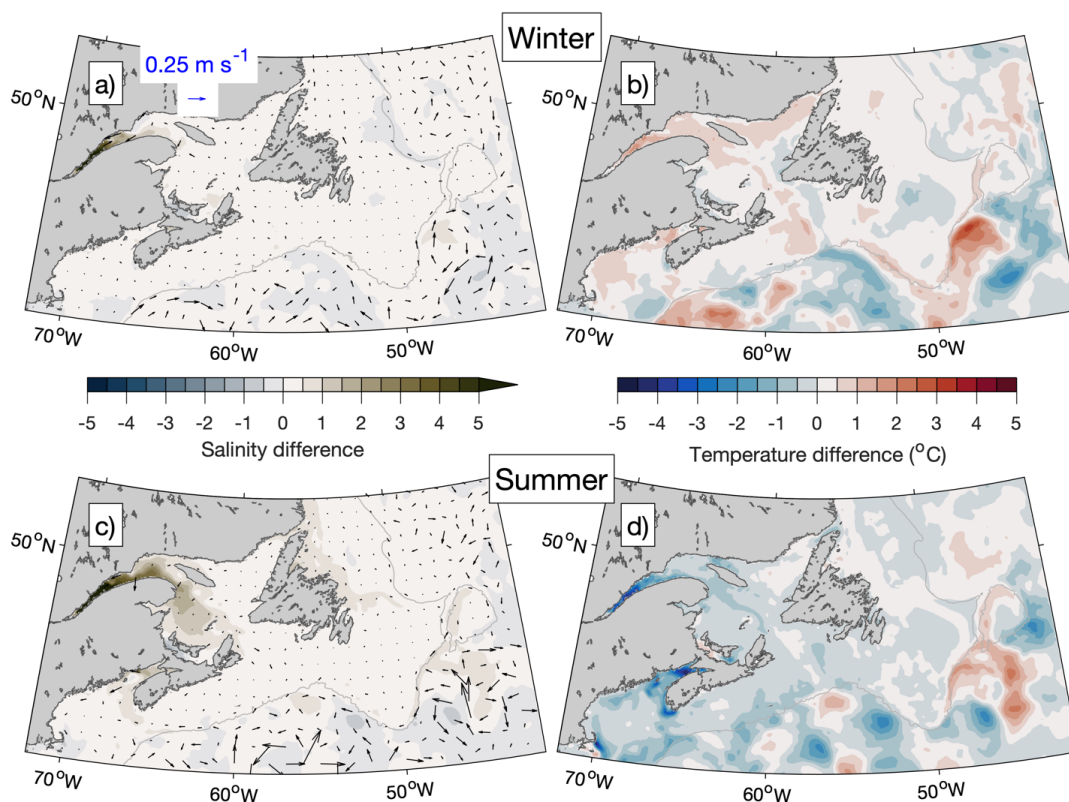
603

**Figure 17.** Differences between Prog and NoTides over Ungava Bay: 2015–2018 averages of seasonal-mean simulated currents (thick magenta arrows: Prog, thin green arrows: NoTides) and temperature difference (Prog minus NoTides) at the sea surface (a, c) and bottom layer (b, d) in winter (a–b) and summer (c–d). Current vectors are shown at every sixth model grid point. The gray contour line represents the 100-m water depth.



604  
605  
606  
607  
608  
609

**Figure 18.** 2015–2018 averages of seasonal-mean sea ice concentrations in Ungava Bay during summer simulated in runs Prog (a) and NoTides (b); seasonal-mean sea surface temperature for summer simulated by runs Prog (c) and NoTides (d).



610  
611  
612

**Figure 19.** Similar to Fig. 17, but for the area between the Gulf of Maine and the southern Labrador Sea.

613 Wang et al. (2020) have suggested, this may be caused by internal tides that are generated near  
614 the shelf break and propagate offshore.

#### 615 4.2 The effect of sea ice

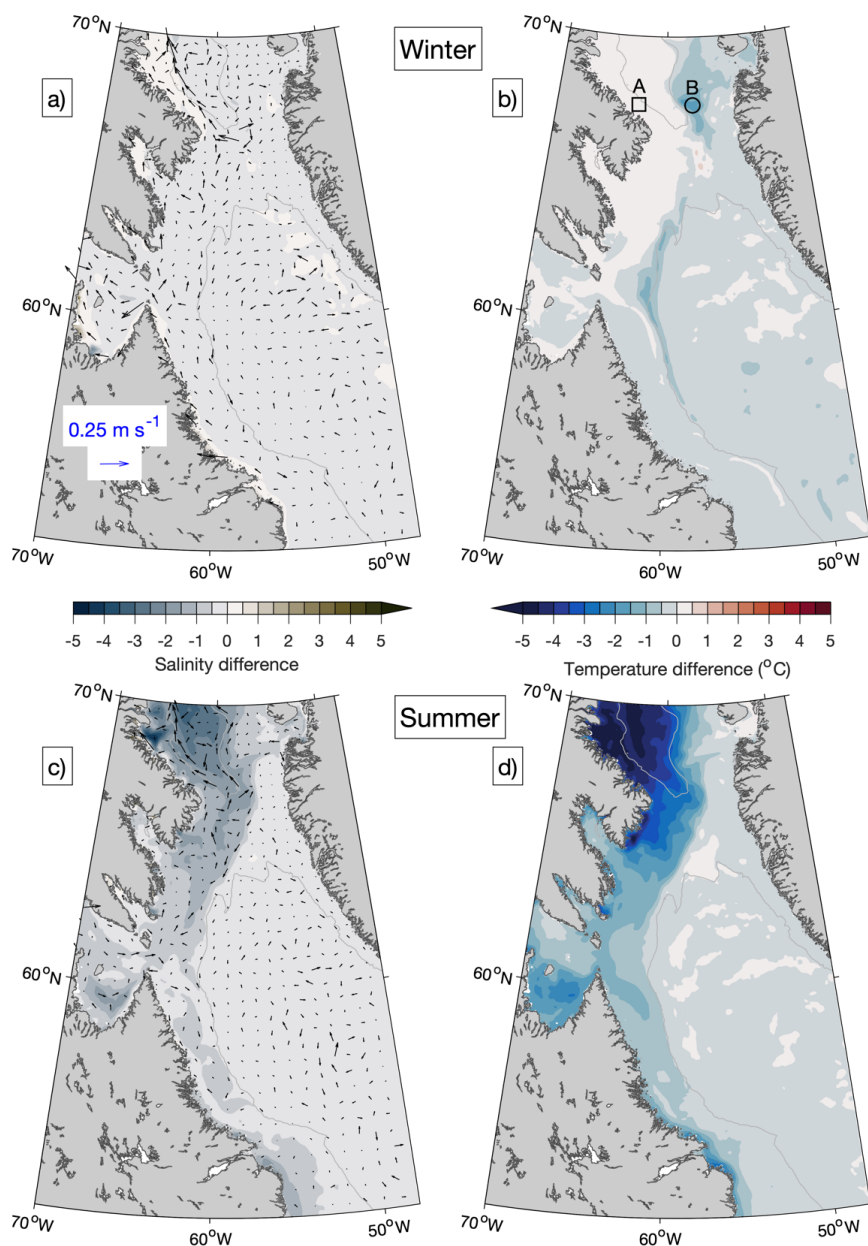
616 The effect of sea ice is examined next by comparing simulated surface fields from Prog to those  
617 from the simulation in which ROMS is run without coupling to CICE (NoIce). A prominent  
618 feature in winter is the horizontal gradient in  $\Delta S_{sfc}^{P-NI}$ , approximately aligned with the 1000-m  
619 isobath, in western Baffin Bay (Fig. 20a).  $\Delta S_{sfc}^{P-NI}$  is positive on the shelf ( $\sim 0.2$ ) but negative  
620 offshore of the shelf break ( $\sim -0.3$ ). In the zone where  $\Delta S_{sfc}^{P-NI}$  changes signs,  $\Delta |\vec{V}|_{sfc}^{P-NI}$  is positive  
621 (up to  $\sim 0.3 \text{ m s}^{-1}$ ). The area on the shelf where  $\Delta S_{sfc}^{P-NI}$  is positive coincides with the highest  
622 average sea ice thickness in the domain (Fig. 10d), which makes the higher salinity in Prog



623 consistent with brine rejection at the time of sea ice formation. Values of  $|\Delta T_{sfc}^{P-NI}|$  in winter (Fig.  
624 20b) tend to be largest over the parts of Baffin Bay and the northern Labrador Shelf where the  
625 ice edge occurs in Prog (Fig. 10c).  $\Delta T_{sfc}^{P-NI}$  in these areas are negative (as low as  $\sim -1.9^\circ$ ). Surface  
626 heat flux is expected to result in positive  $\Delta T_{sfc}^{P-NI}$ , given that in winter it is expected to cool the  
627 ocean surface while sea ice can insulate the ocean surface below from cold air. Another possible  
628 factor in  $\Delta T_{sfc}^{P-NI}$  is vertical mixing, which is examined later.

629 In summer,  $\Delta S_{sfc}^{P-NI}$  and  $\Delta T_{sfc}^{P-NI}$  (Fig. 20c and 20d respectively) are lowest in western Baffin Bay,  
630 with the former as low as  $\sim -4$  (reflecting the input of freshwater due to melting sea ice) and the  
631 latter as low as  $\sim -4.7^\circ\text{C}$  (reflecting the blocking of shortwave radiation by the sea ice that  
632 remains in summer). These results suggest that, as sea ice in areas such as Baffin Bay and the  
633 Labrador Shelf decline in a warming climate, areas downstream from them such as the Scotian  
634 Shelf and the Gulf of Maine will experience changes in the temperature and salinity of the water  
635 that is brought there by the Labrador Current. The effect of changes in water masses advected  
636 into a given area, in combination with changes that occur in situ due to climate change, is  
637 another possible topic of future research.

638 Differences in the wintertime vertical stratification and vertical mixing between Prog and NoIce  
639 are examined further using vertical profiles of four-year mean wintertime temperature, salinity,  
640 and vertical eddy viscosity produced by the two runs, as well as the squared buoyancy frequency  
641 ( $N^2$ ) calculated from the mean wintertime temperature and salinity using the Gibbs-SeaWater  
642 Oceanographic Toolbox (McDougall and Barker, 2011). The profiles represent temporal averages  
643 over the same period as in Figs. 20a–b (winters of 2015–2018) and are calculated at 1-m depth  
644 intervals for two locations: location A ( $62.56^\circ\text{W}$ ,  $67.60^\circ\text{N}$ ), indicated by the square in Fig. 20b,  
645 where  $\Delta T_{sfc}^{P-NI}$  is small and the 2015–2018 mean of the February-mean sea ice cover is  $\sim 95\%$   
646 (Fig. 10c), and location B ( $57.64^\circ\text{W}$ ,  $67.60^\circ\text{N}$ ), indicated by the circle in Fig. 20b, where  
647  $\Delta T_{sfc}^{P-NI}$  has a large magnitude ( $\sim -1.9^\circ\text{C}$ ) and the four-year mean of the February-mean sea ice  
648 cover is  $\sim 84\%$ . The model's water depths at the two locations are similar (231 m and 218 m).



649

650

651

652

653

654

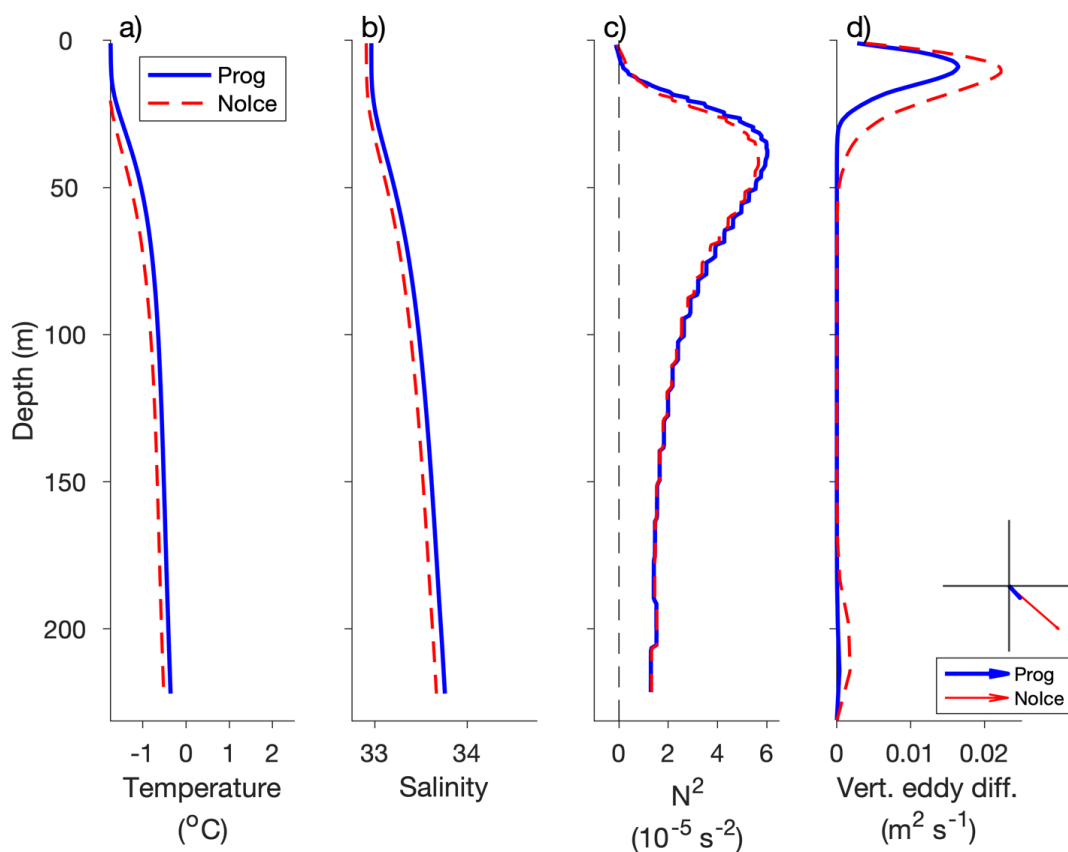
655

**Figure 20.** Differences in seasonal-mean simulated sea surface salinity and currents (**a, c**) and temperature (**b, d**) over Baffin Bay and the Labrador Sea when results of NoIce are subtracted from those of Prog, averaged over winters (**a, b**) and summers (**c, d**) of 2015–2018. Difference vectors are shown at every 12th model grid point. The gray contour line represents the 1000-m water depth. Locations A and B, for which the vertical profiles of model variables are shown in Figs. 21 and 22, are indicated in panel (**b**) with a square and a circle respectively.



656 The vertical profiles of mean wintertime temperature (Fig. 21a) and salinity (Fig. 21b) at location  
657 A are similar between runs Prog and NoIce, with a vertical range of  $<1.4^{\circ}\text{C}$  for temperature and  
658  $<0.8$  for salinity in both runs. The profiles of  $N^2$  (Fig. 21c) are thus also similar between the runs,  
659 with maximum values of  $\sim 6 \times 10^{-5} \text{ s}^{-2}$  about 40 m below the sea surface. Negative values of  $N^2$ ,  
660 indicating instability, are limited to the top few metres of the water column. Values of the  
661 Richardson number (not shown) below 0.25, including negative values, are limited to the top 5 m  
662 of the water column, again indicating a mostly stable water column and weak convection in both  
663 Prog and NoIce. The mean wintertime vertical mixing below the surface is very weak in both  
664 runs (Fig. 21d), with the vertical eddy diffusivity from both runs having maximum values of  
665  $\sim 0.02 \text{ m}^2 \text{ s}^{-1}$  about 10 m below the surface and having values  $<0.002 \text{ m}^2 \text{ s}^{-1}$  in  $\sim 80\%$  of the water  
666 column. It should be noted that the mean wintertime stress exerted on the sea surface (by winds  
667 and/or sea ice in Prog and by winds in NoIce) differs significantly between the two runs (Fig.  
668 21d). The surface stress has a much smaller magnitude in Prog ( $0.02 \text{ N m}^{-2}$ ) than in NoIce ( $1.0 \text{ N}$   
669  $\text{m}^{-2}$ ), which can be explained by the buffering effect of sea ice on the wind stress in Prog. Due to  
670 this buffering effect of sea ice, the wind-induced vertical mixing in the surface layer (Fig. 21d) is  
671 weaker in Prog than in NoIce, as expected.

672 In contrast to location A, the vertical profiles of mean wintertime model results at location B  
673 differ significantly between runs Prog and NoIce. The mean wintertime temperature (Fig. 22a)  
674 has a vertical range of  $>3^{\circ}\text{C}$  in Prog (about  $-0.9^{\circ}\text{C}$  near the surface and  $2.4^{\circ}\text{C}$  near the bottom)  
675 but  $<1^{\circ}\text{C}$  in NoIce (about  $1.1^{\circ}\text{C}$  near the surface and  $1.7^{\circ}\text{C}$  near the bottom). The mean  
676 wintertime salinity (Fig. 22b) has a vertical range of  $\sim 0.5$  in Prog (about 34.0 near the surface  
677 and 34.5 near the bottom) but just  $\sim 0.1$  in NoIce (about 34.5 near the surface and 34.6 near the  
678 bottom). Values of  $N^2$  (Fig. 22c) from both runs are lower than at location A; with a maximum of  
679  $\sim 1.9 \times 10^{-5} \text{ s}^{-2}$  in Prog and  $\sim 2.1 \times 10^{-6} \text{ s}^{-2}$  in NoIce. In addition, the  $N^2$  in NoIce is negative in the  
680 top  $\sim 20$  m of the water column and between depths of  $\sim 40$  and  $\sim 50$  m, indicating unstable  
681 stratification and unrealistically strong convection. The Richardson number is  $<0.25$  in the top  $\sim 5$   
682 m of the water column in Prog, and at approximately the same depths as the negative values of  
683  $N^2$  in NoIce. The maximum vertical eddy diffusivity coefficient is  $\sim 0.3 \text{ m}^2 \text{ s}^{-1}$  in NoIce, which is  
684 much larger than the maximum values of  $\sim 0.06 \text{ m}^2 \text{ s}^{-1}$  in Prog, while the surface stress is similar  
685 at  $\sim 0.1 \text{ N m}^{-2}$  in both runs.

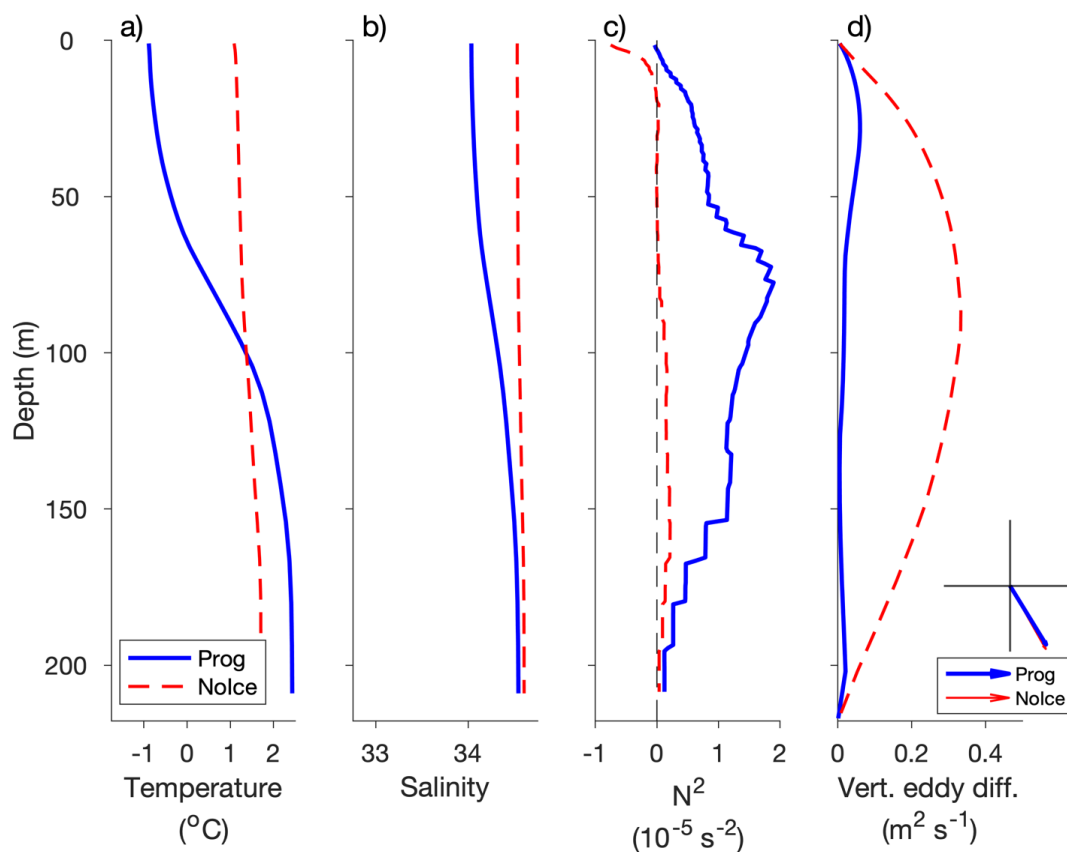


686  
687

688 **Figure 21.** Vertical profiles of wintertime temperature (a), salinity (b), squared buoyancy frequency (c), and vertical  
689 eddy diffusivity (d) simulated by the model in Prog (blue solid line) and NoIce (red dashed line), averaged over  
690 2015–2018, interpolated to 1-m depth intervals, at location A, indicated by the square in Fig. 20b (62.56° W, 67.60°  
691 N). Also shown in panel (d) is the stress exerted on the sea surface by sea ice and/or winds in the Prog (thick arrow)  
692 and NoIce (thin arrow) runs, averaged over the same period as the other fields. The x- and y-axes for the surface  
693 stress range from -0.1 to 0.1 N m<sup>-2</sup>.



694



695

696

697 **Figure 22.** Similar to Fig. 21 but for location B, indicated by the circle in Fig. 20b (57.64° W, 67.60° N). Note the  
 698 change from Fig. 21 in the x-axis limits for the squared buoyancy frequency (c) and the vertical eddy diffusivity (d).

699 A possible explanation for the relatively warm (>2°C) and salty (>34) subsurface water in the  
 700 lower water column at location B in Prog (solid blue lines in Fig. 22a,b) is the horizontal  
 701 advection of relatively warm and salty waters from the south to this location. In Prog, the ocean-  
 702 to-air heat flux in winter results in cooling of the near-surface water as well as sea ice formation,  
 703 and subsurface ablation of the sea ice can be a source of fresh water that contributes to vertical  
 704 stability. The advection of relatively warm, salty subsurface waters from the south would also  
 705 occur in NoIce, but in this case the near-surface water would be cooled to the freezing point  
 706 without an accompanying reduction in salinity, which may explain the very large vertical mixing  
 707 and nearly uniform vertical profiles of temperature and salinity in this run.



## 708 **5 Conclusions**

709 In this study, a newly-developed, fully-coupled modelling system for simulating the ocean  
710 circulation, sea ice, and biogeochemistry of the northwest North Atlantic Ocean (DalROMS-  
711 NWA12 v1.0) was described. The model domain covers the area from Cape Hatteras to Baffin  
712 Bay with a horizontal resolution of ~2 to ~8 km, making this modelling system highly suitable  
713 for a range of research topics, including study of the biological carbon pump and quantification  
714 of the major physical and biogeochemical (BGC) processes influencing the ocean carbon cycle  
715 over the region. The results of two simulations using this modelling system, with and without  
716 nudging of the simulated temperature and salinity towards a blend of observations and  
717 reanalysis, were compared to observations and reanalysis. We found that results of the control  
718 run, which included the nudging, are more realistic than results of the prognostic (un-nudged)  
719 simulation for several important physical features observed in this region, such as separation of  
720 the Gulf Stream and the West Greenland Current from their respective coasts, as well as  
721 propagation of low-salinity waters from the St. Lawrence Estuary. These results demonstrate the  
722 utility of simple data assimilation in reducing the systematic model errors that can be attributed  
723 to model configuration (such as horizontal grid resolution in the case of currents' separation from  
724 coasts and the choice of tracer advection scheme in the case of estuarine plume propagation) and  
725 unresolved or parameterized physical and BGC processes. The prognostic simulation, while  
726 having difficulties with the above-mentioned features, was able to reproduce the general  
727 spatiotemporal patterns of the physical fields and outperformed the control run in terms of the  
728 sea ice concentration. The major differences between the simulations in the sea ice extent  
729 highlight the complex nature of interactions among the atmosphere, ocean, and sea ice.

730 The modelling system was able to reproduce the general patterns of BGC variables over the  
731 northwest Atlantic shelves and in the Labrador Sea. Further validation will include comparisons  
732 with observations made by BGC Argo floats (Johnson and Claustre, 2016). Future work will use  
733 this modelling system to investigate the biological carbon pump in the Labrador Sea including  
734 vertical flux estimates derived from BGC Argo (Wang and Fennel, 2022 and 2023). The addition  
735 of silicate as a state variable will also be tested.

736 As an example of application of this modelling system, sensitivity studies were made in which  
737 results of the prognostic simulation were compared to those from similar simulations from which



738 either the tides or simulation of sea ice were excluded. The comparisons suggest that tides and  
739 sea ice strongly affect the physical oceanography of the NWA in several ways. These include the  
740 combined effects of tides and sea ice (in Ungava Bay) as well as individual effects (e.g., higher  
741 surface salinity in summer when sea ice is not simulated).

742 In addition to studies of the biological carbon pump and of the downstream effects of changes in  
743 the water transported by the Labrador Current, another possible direction of future research is to  
744 use the ocean state simulated by this model as input for numerical particle-tracking experiments  
745 to investigate connectivity among different areas of the NWA. The resulting metrics of  
746 connectivity under current and projected future climate conditions can support decision-making  
747 processes concerning conservation measures. The model will also be used to compare  
748 approaches to reducing bias in long-term simulations (Renkl et al., in prep.).

749 The high air-to-sea flux of CO<sub>2</sub> and the subsequent downward export of fixed carbon make the  
750 NWA a key component in the global climate system, but it is a remote region where seasonal  
751 transitions can take place in just a few weeks (e.g., in terms of pCO<sub>2</sub>; Körtzinger et al., 2008) and  
752 details of the interactions between physical and biogeochemical processes are still unknown or  
753 remain poorly integrated into models (e.g., the sea-ice carbon pump; Richaud et al., 2023). The  
754 four-dimensional ocean states produced by numerical models can aid in the interpretation of  
755 observations as well as enable experiments that elucidate the roles of various processes in the  
756 ocean and how those processes might change under future climate scenarios.

## 757 **Appendix A: The vertical coordinate system in ROMS**

758 ROMS uses a generalized terrain-following vertical coordinate system with several options  
759 for vertical transformation equations and vertical stretching functions. In this study the default  
760 configuration is used, with the vertical coordinate  $S$  defined as (Hedstrom, 2018):

$$761 \quad z(x, y, \sigma, t) = \zeta(x, y, t) + [\zeta(x, y, t) + h(x, y)]S(x, y, \sigma) \quad (\text{A1})$$

$$762 \quad S(x, y, \sigma) = \frac{h_c + h(x, y)C(\sigma)}{h_c + h(x, y)} \quad (\text{A2})$$

$$763 \quad C(\sigma) = \frac{\exp(\theta_B C'(\sigma)) - 1}{1 - \exp(-\theta_B)} \quad (\text{A3})$$

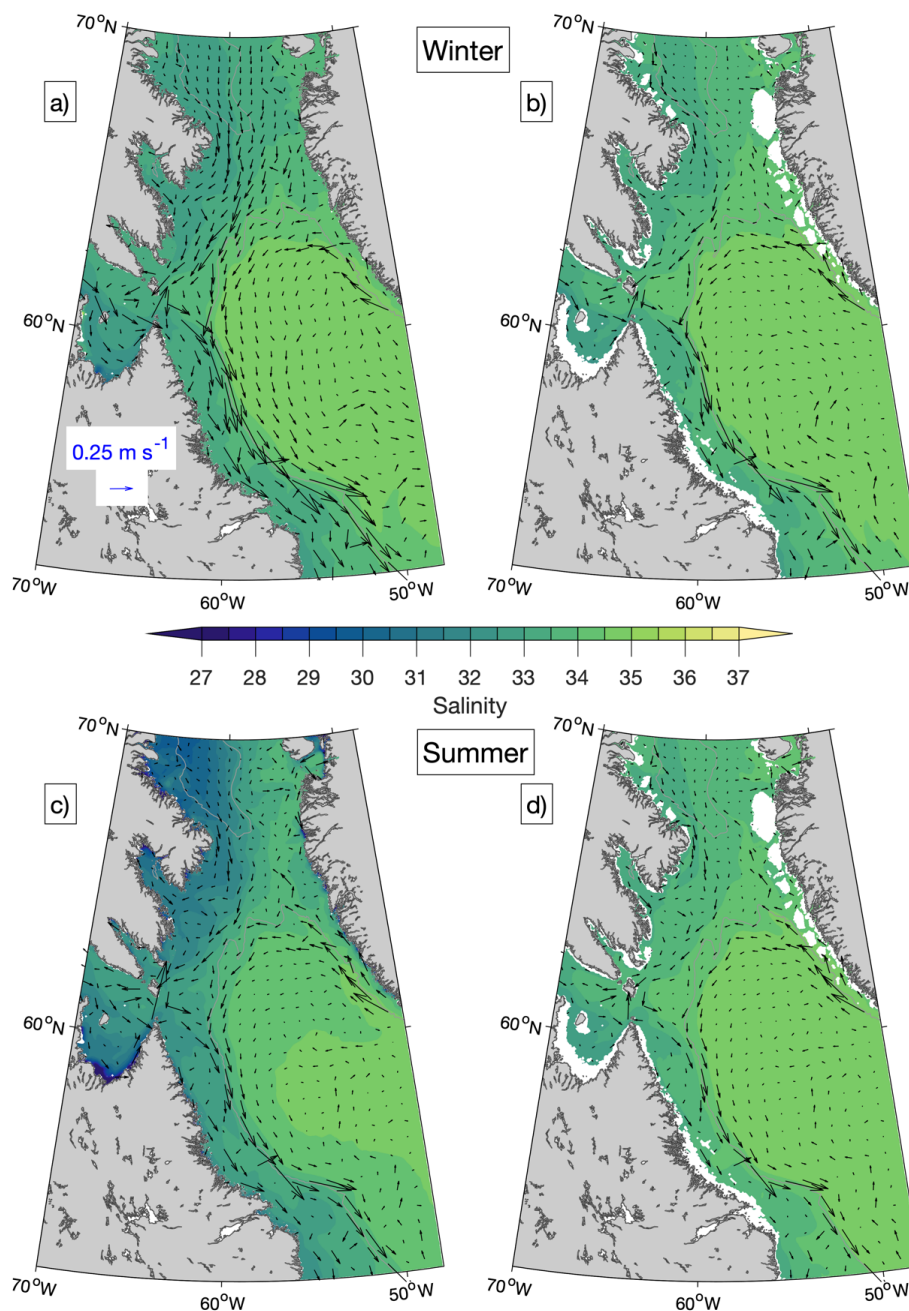
$$764 \quad C'(\sigma) = \frac{1 - \cosh(\theta_S \sigma)}{\cosh(\theta_S) - 1} \quad (\text{A4})$$



765 where  $\sigma$  ranges from 0 at the free surface to -1 at the ocean bottom,  $\zeta$  is the free surface,  $h$  is the  
766 undisturbed water column thickness,  $h_c$  is the value of  $h$  below which the vertical layers are more  
767 uniformly spaced, and  $\theta_s$  and  $\theta_b$  are parameters that control the vertical resolution near the  
768 surface and the bottom respectively. In this study ROMS has 40 layers and the parameters  $h_c$ ,  $\theta_s$ ,  
769 and  $\theta_b$  are set to 100 m, 5.0, and 0.5 respectively.

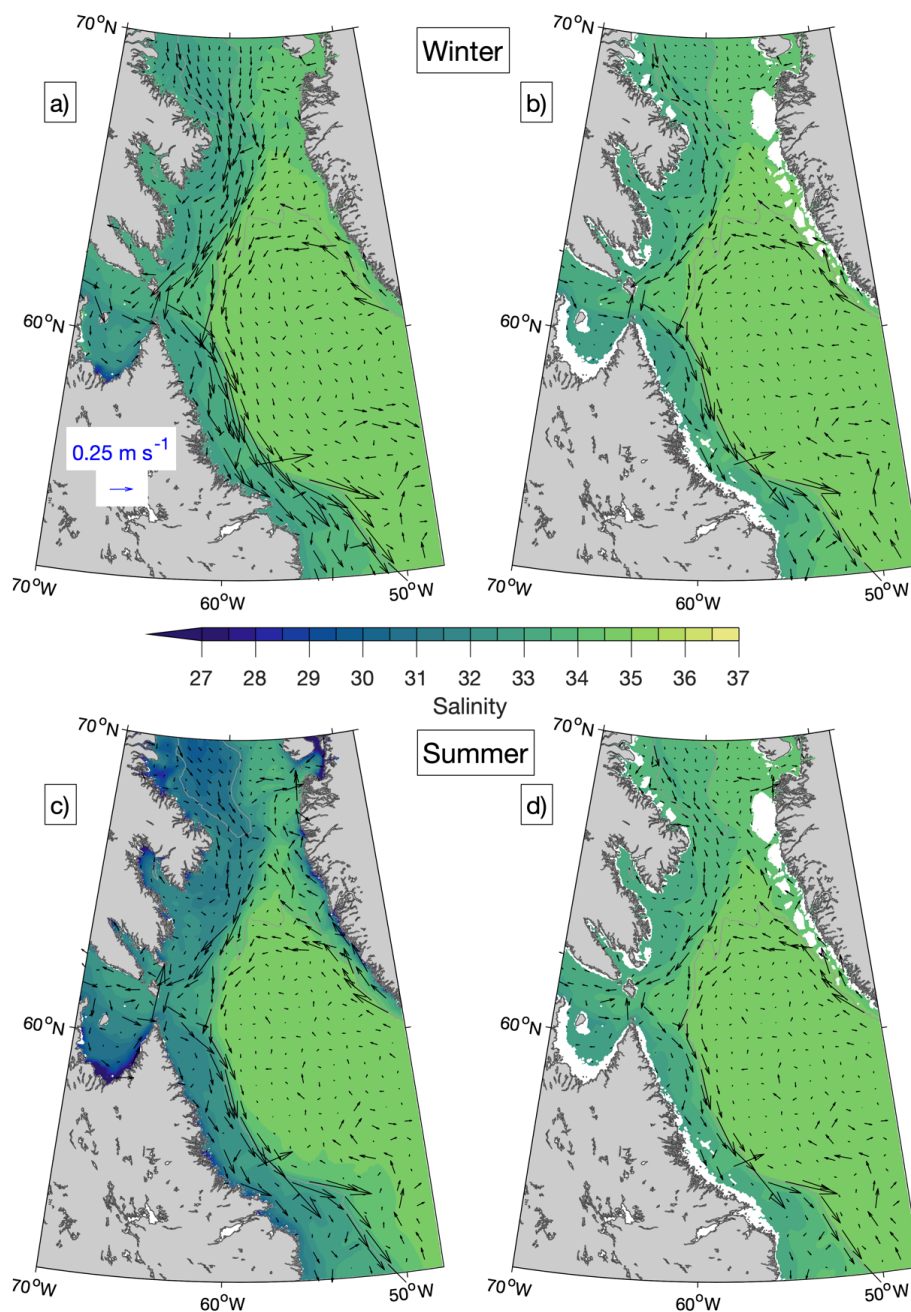
## 770 **Appendix B: Seasonal-mean simulated fields**

771 Seasonal means of salinity and currents in Baffin Bay and the northern Labrador Sea  
772 simulated in Ctrl and Prog, averaged over December 2014–December 2018, are shown in Figs.  
773 B1 and B2. Differences between the simulations are more evident in summer (June–August;  
774 Figs. B1c–d and B2c–d) than in winter (December–February; Figs. B1a–b and B2a–b). The  
775 northward branch of the West Greenland Current and the Baffin Island Current are stronger in  
776 Prog by up to  $\sim 0.25 \text{ m s}^{-1}$  at the surface and  $\sim 0.15 \text{ m s}^{-1}$  for model results interpolated to the 100-  
777 m depth. In the area between the southern Labrador Sea and the Gulf of Maine (Figs. B3 and  
778 B4), the difference in salinity between the simulations is more prominent in summer, following  
779 the annual peak in freshwater discharges from the St. Lawrence and other rivers. In the St.  
780 Lawrence Estuary, the 2015–2018 mean of summer surface salinity simulated in Prog is lower  
781 than that from Ctrl by up to  $\sim 3.5$ , but further downstream in the Gulf of St. Lawrence, the  
782 salinity from Prog is higher by  $\sim 2$ .



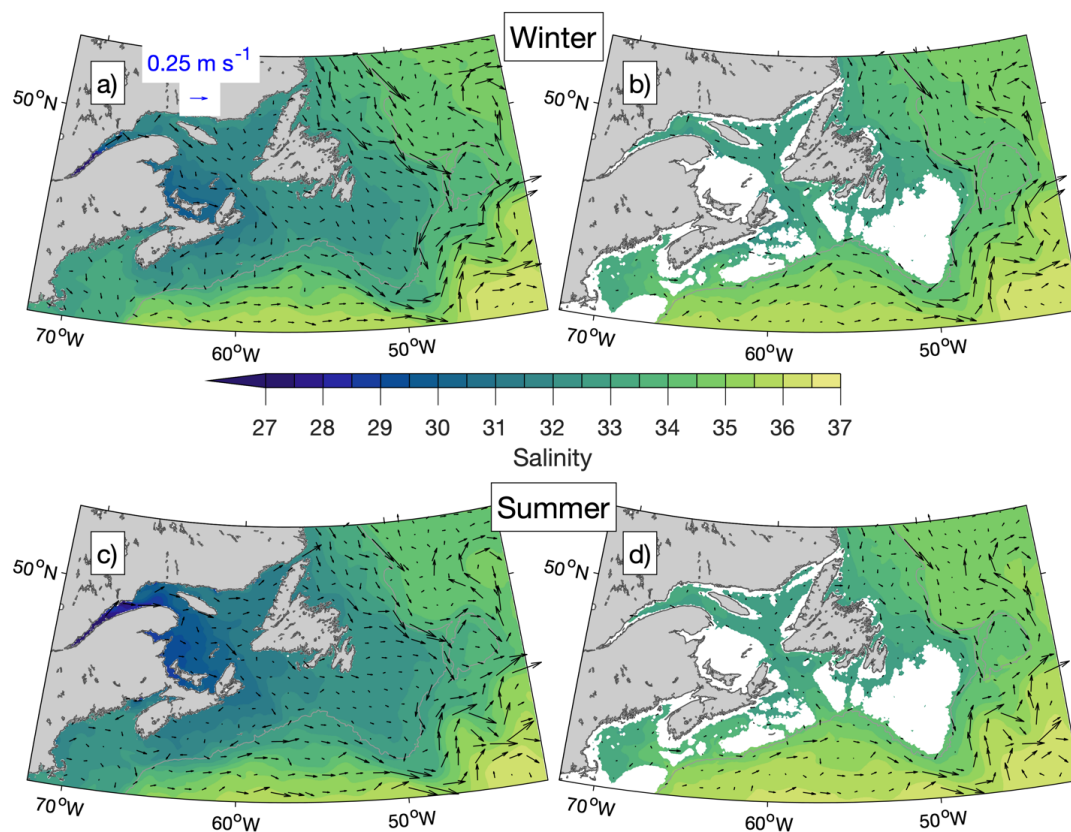
783  
784  
785  
786  
787  
788

**Figure B1.** Seasonal-mean simulated salinity and currents at the sea surface (a, c) and interpolated to the 100-m depth (b, d) from Ctrl averaged over the winters (a, b) and summers (c, d) of 2015–2018 in Baffin Bay and the Labrador Sea. Winters are defined as December of the previous year to February of that year. Summers are defined as June to August. Current vectors are shown at every 12th grid point. The 1000-m depth contour is shown in gray.



789  
790  
791

Figure B2. Similar to Figure B1 but for Prog.



792

793

794

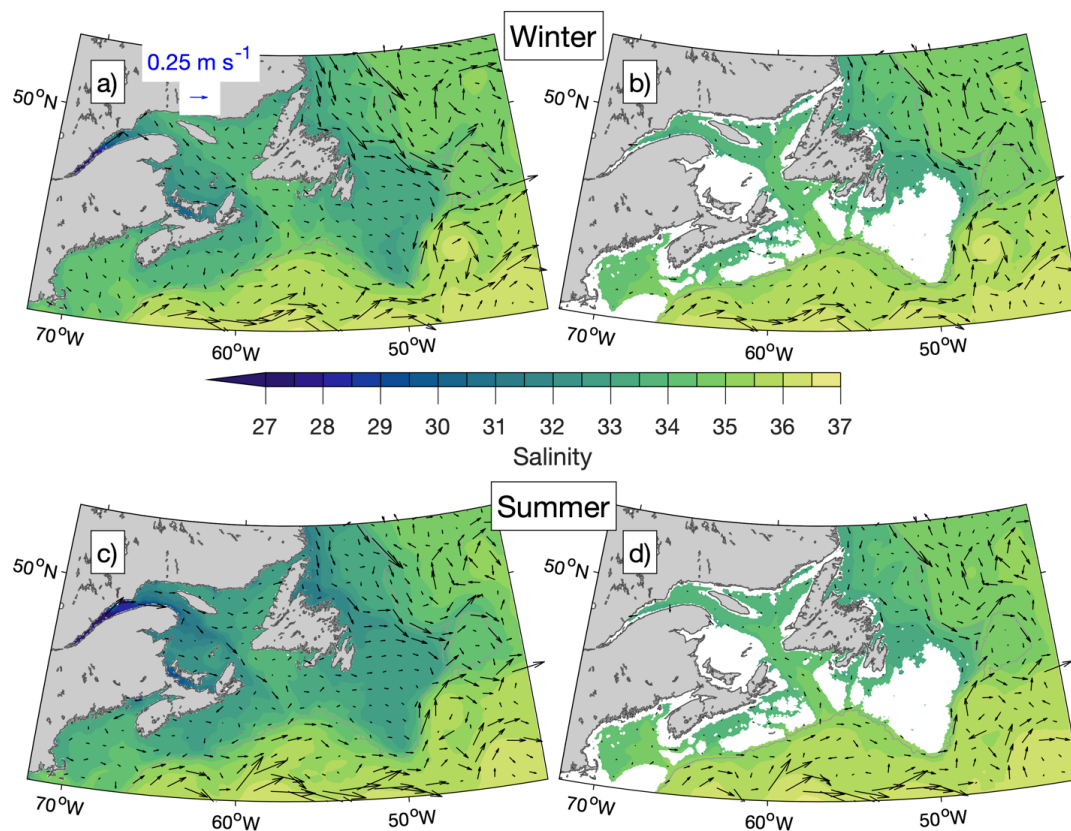
795

796

**Figure B3.** Seasonal-mean simulated salinity and currents at the sea surface (**a, c**) and interpolated to the 100-m depth (**b, d**) from Ctrl averaged over the winters (**a, b**) and summers (**c, d**) of 2015–2018 over the area between the Gulf of Maine and the southern Labrador Sea. Current vectors are shown at every 12th grid point. The 1000-m depth contour is shown in gray.



797



798

799

800

**Figure B4.** Similar to Fig. B3 but for Prog.

### 801 **Appendix C: Datasets used in model performance assessment**

802 Online sources of the datasets used to assess the model performance are listed below in the order  
803 they are discussed in Section 3.

- 804 1. Sea surface temperature: OISST v2.1 (Huang et al., 2021), a daily dataset on a  $1/4^\circ$  grid that  
805 incorporates satellite and in situ observations. A combination of v2.0 and v2.1 was used in this  
806 study; v2.0 is now retired. <https://www.ncei.noaa.gov/products/optimum-interpolation-sst>
- 807 2. Sea surface salinity: MULTI-OBS\_GLO\_PHY\_S\_SURFACE\_MYNRT\_015\_013 (Buongiorno  
808 Nardelli et al., 2016), a dataset that incorporates satellite and in situ observations. At the time  
809 of this study, it was a weekly dataset on a  $1/4^\circ$  grid; now it is a daily dataset on a  $1/8^\circ$  grid.



- 810 [https://data.marine.copernicus.eu/product/MULTIOBS\\_GLO\\_PHY\\_S\\_SURFACE\\_MYNRT](https://data.marine.copernicus.eu/product/MULTIOBS_GLO_PHY_S_SURFACE_MYNRT)  
811 [015\\_013/description](https://data.marine.copernicus.eu/product/MULTIOBS_GLO_PHY_S_SURFACE_MYNRT_015_013/description)
- 812 3. **Currents**: GLOBAL\_MULTIYEAR\_PHY\_001\_030, also known as GLORYS12V1  
813 (Lellouche et al., 2021), a daily reanalysis dataset on a 1/12° grid.  
814 [https://data.marine.copernicus.eu/product/GLOBAL\\_MULTIYEAR\\_PHY\\_001\\_030/description](https://data.marine.copernicus.eu/product/GLOBAL_MULTIYEAR_PHY_001_030/description)  
815 [on](https://data.marine.copernicus.eu/product/GLOBAL_MULTIYEAR_PHY_001_030/description)
- 816 4. **Shipboard observations of physical and biogeochemical variables**: Atlantic Zone Monitoring  
817 Program (Pepin et al., 2005) cruises take place seasonally and Atlantic Zone Off-Shelf  
818 Monitoring Program (e.g., Yashayaev and Loder, 2017) cruises take place annually.  
819 [https://catalogue.cioosatlantic.ca/dataset/ca-cioos\\_9a4bd73f-12a2-40ff-a7c7-b961a1d11311](https://catalogue.cioosatlantic.ca/dataset/ca-cioos_9a4bd73f-12a2-40ff-a7c7-b961a1d11311)  
820 [https://catalogue.cioosatlantic.ca/dataset/ca-cioos\\_15f90eab-21ed-447d-aea7-8fe98ea27fe5](https://catalogue.cioosatlantic.ca/dataset/ca-cioos_15f90eab-21ed-447d-aea7-8fe98ea27fe5)
- 821 5. **Sea ice**: AMSR2 ASI sea ice concentration data for the Arctic, v5.4 (Melsheimer and Spreen,  
822 2019), a daily dataset on a 6.5-km grid derived from satellite observations.  
823 <https://doi.pangaea.de/10.1594/PANGAEA.898399>

## 824 **Code and Data Availability**

825 The model codes, scripts for compiling the model, and sample CPP header and runtime  
826 parameter files for physics-only simulations are available at  
827 <https://doi.org/10.5281/zenodo.12752091> (Ohashi et al., 2024a). Input files used by the ocean  
828 circulation and sea ice modules in a simulation of September – December 2013 are available at  
829 <https://doi.org/10.5281/zenodo.12752190> (Ohashi et al., 2024b),  
830 <https://doi.org/10.5281/zenodo.12734049> (Ohashi et al., 2024c), and  
831 <https://doi.org/10.5281/zenodo.12735153> (Ohashi et al., 2024d). Daily-mean output files from  
832 the ocean circulation, sea ice, and biogeochemistry modules are available for September 2013  
833 (beginning of simulation period) at <https://doi.org/10.5281/zenodo.12744506> (Ohashi et al.,  
834 2024e) and for January 2015 (beginning of model validation period) at  
835 <https://doi.org/10.5281/zenodo.12746262> (Ohashi et al., 2024f). Input and output files for the  
836 remainder of the simulation period, as well as CPP header, runtime parameter, and input files for  
837 the biogeochemistry module, are available from the corresponding author KO upon request.



838 **Author contributions**

839 KO configured the ocean circulation model; prepared the model bathymetry, freshwater input  
840 files, atmospheric forcing files, and some of the lateral boundary input files; and carried out the  
841 Prog, NoTides, and NoIce runs. AL prepared input files for and configured the biogeochemical  
842 module; and carried out the Ctrl run. CR configured the sea ice model and its coupling to the  
843 ocean circulation model; prepared some of the lateral boundary input files and the pseudo-mean  
844 versions of freshwater input files; configured the regions used to evaluate model performance;  
845 processed the observations used in model evaluation; and calculated the model errors with  
846 respect to AZMP observations. AL carried out the analyses for and prepared Figs. 13–15; and  
847 wrote the text describing the biogeochemical module, the Ctrl run, and Figs.13–15. KO prepared  
848 the rest of the manuscript with advice from JS. JS, KF, and EO provided advice throughout  
849 development and evaluation of the model and provided funding to KO, AL, and CR respectively.

850 **Competing interests**

851 The authors declare that they have no conflicts of interest.

852 **Acknowledgements**

853 This study is part of the Ocean Frontier Institute’s research project “The Northwest Atlantic  
854 Biological Carbon Pump”. Simulations were carried out on computing resources maintained by  
855 the Digital Research Alliance of Canada. JS, KF, and EO acknowledge support from the National  
856 Science and Engineering Research Council of Canada’s Discovery Grant program. JS and KO  
857 were supported by funding from Fisheries and Oceans Canada (for the project “Modelling  
858 ecological connectivity among Canada’s Atlantic Marine Protected Areas during the  
859 Anthropocene”) during preparation of this manuscript. CR was supported by a postdoctoral  
860 fellowship from the Marine Environmental Observation, Prediction and Response network  
861 (MEOPAR). The authors thank Fehmi Dilmahamod, Xianmin Hu, Bin Wang, and Shengmu Yang  
862 for their suggestions and assistance during development of the model. The colour maps used in  
863 this study are by Thyng et al. (2016) and Crameri (2018).



## 864 References

- 865 Allen, J. S., Newberger, N. A., and Federiuk, J.: Upwelling circulation on the Oregon continental shelf. Part I:  
866 Response to idealized forcing, *J. Phys. Oceanogr.*, 25(8), 1843–1866, [https://doi.org/10.1175/1520-0485\(1995\)025%3C1843:UCOTOC%3E2.0.CO;2](https://doi.org/10.1175/1520-0485(1995)025%3C1843:UCOTOC%3E2.0.CO;2), 1995.
- 867  
868
- 869 Babb, D. G., Kirillov, S., Galley, R. J., Straneo, F., Ehn, J. K., Howell, S. E. L., Brady, M., Ridenour, N. A., and  
870 Barber, D. G.: Sea ice dynamics in Hudson Strait and its impact on winter shipping operations, *J. Geophys. Res.-*  
871 *Oceans*, 126, e2021JC018024, <https://doi.org/10.1029/2021JC018024>, 2021.
- 872
- 873 Bamber, J. L., Tedstone, A. J., King, M. D., Howat, I. M., Enderlin, E. M., van den Broeke, M. R., and Noel, B.:  
874 Land ice freshwater budget of the Arctic and North Atlantic Oceans: 1. Data, methods, and results, *J. Geophys.*  
875 *Res.-Oceans*, 123, <https://doi.org/10.1002/2017JC013605>, 2018.
- 876
- 877 Bitz, C. M. and Lipscomb, W. H.: An energy-conserving thermodynamic model of sea ice, *J. Geophys. Res.*,  
878 104(C7), 15669–15677, <https://doi.org/10.1029/1999JC900100>, 1999.
- 879
- 880 Bouillon, S., Fichefet, T., Legat, V., and Madec, G.: The elastic-viscous-plastic method revisited, *Ocean Model.*, 71,  
881 2–12, <https://doi.org/10.1016/j.ocemod.2013.05.013>, 2013.
- 882
- 883 Bourgault, D. and Koutitonsky, V. G.: Real-time monitoring of the freshwater discharge at the head of the St.  
884 Lawrence Estuary, *Atmos.-Ocean*, 37(2), 203–220, <https://doi.org/10.1080/07055900.1999.9649626>, 1999.
- 885
- 886 Briegleb, B. P. and Light, B.: A Delta-Eddington multiple scattering parameterization for solar radiation in the sea  
887 ice component of the Community Climate System Model, National Center for Atmospheric Research,  
888 <https://doi.org/10.5065/D6B27S71>, 2007.
- 889
- 890 Buongiorno Nardelli, B., Droghei, R., and Santoleri, R.: Multi-dimensional interpolation of SMOS sea surface  
891 salinity with surface temperature and in situ salinity, *Remote Sens. Environ.*, 180, 392–402,  
892 <https://doi.org/10.1016/j.rse.2015.12.052>, 2016.
- 893
- 894 Cabanes, C., Grouazel, A., von Schuckmann, K., Hamon, M., Turpin, V., Coataoan, C., Paris, F., Guinehut, S.,  
895 Boone, C., Ferry, N., de Boyer Montégut, C., Carval, T., Reverdin, G., Pouliquen, S., and Le Traon, P.-Y.: The  
896 CORA dataset: validation and diagnostics of in-situ ocean temperature and salinity measurements, *Ocean Sci.*, 9,  
897 1–18, <https://doi.org/10.5194/os-9-1-2013>, 2013.
- 898
- 899 Chapman, D. C.: Numerical treatment of cross-shelf open boundaries in a barotropic coastal ocean model, *J. Phys.*  
900 *Oceanogr.*, 15, 1060–1075, [https://doi.org/10.1175/1520-0485\(1985\)015%3C1060:NTOCSO%3E2.0.CO;2](https://doi.org/10.1175/1520-0485(1985)015%3C1060:NTOCSO%3E2.0.CO;2), 1985.
- 901
- 902 Chassignet, E. P. and Xu, S.: Impact of horizontal resolution ( $1/12^\circ$  to  $1/50^\circ$ ) on Gulf Stream separation, penetration,  
903 and variability, *J. Phys. Oceanogr.*, 47(8), 1999–2021, <https://doi.org/10.1175/JPO-D-17-0031.1>, 2017.
- 904
- 905 Chelton, D., DeSzoeke, R. A., Schlax, M. G., El Naggar, K., and Siwertz, N.: Geographical variability of the first  
906 baroclinic Rossby radius of deformation. *J. Phys. Oceanogr.*, 28(3), 433–460, [https://doi.org/10.1175/1520-0485\(1998\)028%3C0433:GVOTFB%3E2.0.CO;2](https://doi.org/10.1175/1520-0485(1998)028%3C0433:GVOTFB%3E2.0.CO;2), 1998.
- 907  
908
- 909 Chen, K. and He, R.: Mean circulation in the coastal ocean off northeastern North America from a regional-scale  
910 ocean model. *Ocean Sci.*, 11, 503–517, <https://doi.org/10.5194/os-11-503-2015>, 2015.
- 911
- 912 Cramer, F.: Scientific colour maps [software], Zenodo, <https://doi.org/10.5281/zenodo.1243862>, 2018.
- 913
- 914 Dai, A.: Dai and Trenberth Global River Flow and Continental Discharge Dataset [data set],  
915 <https://doi.org/10.5065/D6V69H1T>, 2017.
- 916
- 917 Drinkwater, K.: On the mean and tidal currents in Hudson Strait, *Atmos.-Ocean*, 26(2), 252–266,  
918 <https://doi.org/10.1080/07055900.1988.9649302>, 1988.



- 919  
920 Dupont, F., Higginson, S., Bourdalle-Badie, R., Lu, Y., Roy, F., Smith, G. C., Lemieux, J.-F., Garric, G., and  
921 Davidson, F.: A high-resolution ocean and sea-ice modelling system for the Arctic and North Atlantic oceans,  
922 *Geosci. Model Dev.*, 8, 1577–1594, <https://doi.org/10.5194/gmd-8-1577-2015>, 2015.
- 923  
924 Egbert, G. D. and Erofeeva, S. Y.: Efficient inverse modeling of barotropic ocean tides, *J. Atmos. Ocean Tech.*, 19,  
925 183–204, [https://doi.org/10.1175/1520-0426\(2002\)019%3C0183:EIMOBO%3E2.0.CO;2](https://doi.org/10.1175/1520-0426(2002)019%3C0183:EIMOBO%3E2.0.CO;2), 2002.
- 926  
927 Ezer, T. and Mellor, G. L.: A generalized coordinate ocean model and a comparison of the bottom boundary layer  
928 dynamics in terrain-following and in  $z$ -level grids, *Ocean Model.*, 6, 379–403, [https://doi.org/10.1016/S1463-](https://doi.org/10.1016/S1463-5003(03)00026-X)  
929 [5003\(03\)00026-X](https://doi.org/10.1016/S1463-5003(03)00026-X), 2004.
- 930  
931 Fairall, C. W., Bradley, E. F., Godfrey, J. S., Wick, G. A., Edson, J. B., and Young, G. S.: Cool-skin and warm-layer  
932 effects on sea surface temperature, *J. Geophys. Res.*, 101(C1), 1295–1308, <https://doi.org/10.1029/95JC03190>,  
933 1996a.
- 934  
935 Fairall, C. W., Bradley, E. F., Rogers, D. P., Edson, J. B., and Young, G. S.: Bulk parameterization of air-sea fluxes  
936 for Tropical-Ocean Global Atmosphere Coupled-Ocean Atmosphere Ocean Experiment, *J. Geophys. Res.*,  
937 101(C2), 3747–3764, <https://doi.org/10.1029/95JC03205>, 1996b.
- 938  
939 Fennel, K., Mattern, J. P., Doney, S., Bopp, L., Moore, A., Wang, B., Yu, L., Ocean biogeochemical modelling, *Nat.*  
940 *Rev. Methods Primers*, 2, 76, <https://doi.org/10.1038/s43586-022-00154-2>, 2022.
- 941  
942 Fennel, K., Wilkin, J., Levin, J., Moisan, J., O'Reilly, J., and Haidvogel, D.: Nitrogen cycling in the Middle Atlantic  
943 Bight: Results from a three-dimensional model and implications for the North Atlantic nitrogen budget, *Global*  
944 *Biogeochem. Cy.*, 20, GB3007, <https://doi.org/10.1029/2005GB002456>, 2006.
- 945  
946 Fennel, K., Wilkin, J., Previdi, M., and Najjar, R.: Denitrification effects on air-sea CO<sub>2</sub> flux in the coastal ocean:  
947 Simulations for the northwest North Atlantic, *Geophys. Res. Lett.*, 35, L24608,  
948 <https://doi.org/10.1029/2008GL36147>, 2008.
- 949  
950 Fennel, K., Hu, J., Laurent, A., Marta-Almeida, M., and Hetland, R.: Sensitivity of hypoxia predictions for the  
951 north- ern Gulf of Mexico to sediment oxygen consumption and model nesting, *J. Geophys. Res.-Oceans*, 118,  
952 990–1002, <https://doi.org/10.1002/jgrc.20077>, 2013.
- 953  
954 Frajka-Williams, E. and Rhines, P. B.: Physical controls and interannual variability of the Labrador Sea spring  
955 phytoplankton bloom in distinct regions, *Deep-Sea Res. Pt. I*, 57, 541–552,  
956 <https://doi.org/10.1016/j.dsr.2010.01.003>, 2010. Garçon, V. C., Oschlies, A., Doney, S. C., McGillicuddy, D.,  
957 Waniek, J.: The role of mesoscale variability on plankton dynamics in the North Atlantic, *Deep-Sea Res. Pt. II*, 48,  
958 2199–2226, [https://doi.org/10.1016/S0967-0645\(00\)00183-1](https://doi.org/10.1016/S0967-0645(00)00183-1), 2001.
- 959  
960 Gatién, M. G.: A study in the slope water region south of Halifax, *J. Fish. Res. Board Can.*, 33(10), 2213–2217,  
961 <https://doi.org/10.1139/f76-270>, 1976.
- 962  
963 GEBCO Compilation Group: GEBCO 2019 Grid [data set], [https://doi.org/10.5285/836f016a-33be-6ddc-e053-](https://doi.org/10.5285/836f016a-33be-6ddc-e053-6c86abc0788e)  
964 [6c86abc0788e](https://doi.org/10.5285/836f016a-33be-6ddc-e053-6c86abc0788e), 2019.
- 965  
966 Haidvogel, D. B., Arango, H., Budgell, W. P., Cornuelle, B. D., Curchister, E., Di Lorenzo, E., Fennel, K., Geyer, W.  
967 R., Hermann, A. J., Lanerolle, L., Levin, J., McWilliams, J. C., Miller, A. J., Moore, A. M., Powell, T. M.,  
968 Shepetchkin, A. F., Sherwood, C. R., Signell, R. P., Warner, and Wilkin, J.: Ocean forecasting in terrain-following  
969 coordinates: Formulation and skill assessment of the Regional Ocean Modeling System, *J. Comput. Phys.*, 227,  
970 3595–3624, <https://doi.org/10.1016/j.jcp.2007/06.016>, 2008.
- 971  
972 Han, G., Hannah, C. G., Loder, J. W., and Smith, P. C.: Seasonal variation of the three-dimensional mean circulation  
973 over the Scotian Shelf, *J. Geophys. Res.*, 102(C1), 1011–1025, <https://doi.org/10.1029/96JC03285>, 1997.
- 974



- 975 Hedstrom, K. S.: Technical manual for a coupled sea-ice/ocean circulation model (Version 5), U.S. Dept. of the  
976 Interior, Bureau of Ocean Energy Management, Alaska OCS Region, 2018.  
977
- 978 Hersbach, H., Bell, B., Berrisford, P., Biavati, G., Horányi, A., Muñoz Sabater, J., Nicolas, J., Peubey, C., Radu, R.,  
979 Rozum, I., Schepers, D., Simmons, A., Soci, C., Dee, D., Thépaut, J.-N.: ERA5 hourly data on single levels from  
980 1979 to present [data set], Copernicus Climate Change Service Climate Data Store,  
981 <https://doi.org/10.24381/cds.adbb2d47>, 2018.  
982
- 983 Huang, B., Liu, C., Banzon, V., Freeman, E., Graham, G., Hankins, B., Smith, T., and Zhang, H.-M.: Improvements  
984 of the Daily Optimum Interpolation Sea Surface Temperature (DOISST) Version 2.1, *J. Climate*, 34, 2923–2939,  
985 <https://doi.org/10.1175/JCLI-D-20-0166.1>, 2021.  
986
- 987 Hunke, E. C. and Dukowicz, J. K.: An elastic-viscous-plastic model for sea ice dynamics, *J. Phys. Oceanogr.*, 27,  
988 1849–1867, [https://doi.org/10.1175/1520-0485\(1997\)027%3C1849:AEVPMF%3E2.0.CO;2](https://doi.org/10.1175/1520-0485(1997)027%3C1849:AEVPMF%3E2.0.CO;2), 1997.  
989
- 990 Hunke, E. C., Lipscomb, W. H., Turner, A. K., Jeffery, N., and Elliott, S.: CICE: The Los Alamos sea ice model  
991 documentation and software user’s manual version 5.1 LA-CC-06-012, Los Alamos National Laboratory, 2015.  
992
- 993 Ikeda, M., Yao, T., and Yao, Q.: Seasonal evolution of sea ice cover and shelf water off Labrador simulated in a  
994 coupled ice-ocean model, *J. Geophys. Res.*, 101(C7), 16465–16489, <https://doi.org/10.1029/96JC00716>, 1996.  
995
- 996 Jacob, R., Larson, J., and Ong, E.: M x N communication and parallel interpolation in Community Climate System  
997 Model version 3 using the Model Coupling Toolkit, *Int. J. High Perform. Comput. Appl.*, 19(3), 293–307,  
998 <https://doi.org/10.1177/1094342005056116>, 2005.  
999
- 1000 Jin, M., Deal, C., Maslowski, W., Matrai, P., Roberts, A., Osinski, R., Lee, Y. J., Frants, M., Elliott, S., Jefferey, N.,  
1001 Hunke, E., and Wang, S.: Effects of model resolution and ocean mixing on forced ice-ocean physical and  
1002 biogeochemical simulations using global and regional system models, *J. Geophys. Res.-Oceans*, 123, 358–377,  
1003 <https://doi.org/10.1002/2017JC013365>, 2018.  
1004
- 1005 Johnson, K. S. and Claustre, H.: Bringing biogeochemistry into the Argo age, *Eos*, 97,  
1006 <https://doi.org/10.1029/2016EO062427>, 2016.  
1007
- 1008 Killworth, P. D.: Time interpolation of forcing fields in ocean models, *J. Phys. Oceanogr.*, 26(1), 136–143,  
1009 [https://doi.org/10.1175/1520-0485\(1996\)026%3C0136:TIOFFI%3E2.0.CO;2](https://doi.org/10.1175/1520-0485(1996)026%3C0136:TIOFFI%3E2.0.CO;2).  
1010
- 1011 Körtzinger, A., Send, U., Wallace, D. W. R., Karstensen, J., and DeGrandpre, M.: Seasonal cycle of O<sub>2</sub> and PCO<sub>2</sub> in  
1012 the central Labrador Sea: Atmospheric, biological, and physical implications, *Global Biogeochem. Cy.*, 22,  
1013 GB1014, <https://doi.org/10.1029/2007GB003029>, 2008.  
1014
- 1015 Kristensen, N. M., Debernard, J. B., Maartenson, S., Wang, K., and Hedstrom, K.: metno/metroms: Version 0.3 -  
1016 before merge (v0.3) [code], Zenodo, <https://doi.org/10.5281/zenodo.1046114>, 2017.  
1017
- 1018 Larson, J., Jacob, R., Ong, E.: The Model Coupling Toolkit: A new Fortran90 toolkit for building Multiphysics  
1019 parallel coupled models, *Int. J. High Perform. Comput. Appl.*, 19(3), 277–292,  
1020 <https://doi.org/10.1177/1094342005056115>, 2005.  
1021
- 1022 Laurent, A., Fennel, K., and Kuhn, A.: An observation-based evaluation and ranking of historical Earth system  
1023 model simulations in the northwest North Atlantic Ocean, *Biogeosciences*, 18, 1803–1822,  
1024 <https://doi.org/10.5194/bg-18-1803-2021>, 2021.  
1025
- 1026 Lauvset, S. K., Lange, N., Tanhua, T., Bittig, H. C., Olsen, A., Kozyr, A., Álvarez, M., Becker, S., Brown, P. J.,  
1027 Carter, B. R., Cotrim da Cunha, L., Feely, R. A., van Heuven, S., Hoppema, M., Ishii, M., Jeansson, E.,  
1028 Jutterström, S., Jones, S. D., Karlsen, M. K., Lo Monaco, C., Michaelis, P., Murata, A., Pérez, F. F., Pfeil, B.,  
1029 Schirnick, C., Steinfeldt, R., Suzuki, T., Tilbrook, B., Velo, A., Wanninkhov, R., Woosley, R. J., and Key, R. M.:



- 1030 An updated version of the global interior ocean biogeochemical data product, GLODAPv2.2021, *Earth Syst. Sci.*  
1031 *Data*, 13, 5565–5589, <https://doi.org/10.5194/essd-13-5565-2021>, 2021.
- 1032
- 1033 Lavoie, D., Lambert, N., Starr, M., Chassé, J., Riche, O., Le Clainche, Y., Azetsu-Scott, K., Béjaoui, B., Christian, J.  
1034 R., and Gilbert, D.: The Gulf of St. Lawrence Biogeochemical Model: A management tool for fisheries and ocean  
1035 management, *Front. Mar. Sci.*, 8, 732269, <https://doi.org/10.3389/fmars.2021.732269>, 2021.
- 1036
- 1037 Le Fouest, V., Zakardjian, B., and Saucier, F. J.: Plankton ecosystem response to freshwater-associated bulk turbidity  
1038 in the subarctic Gulf of St. Lawrence (Canada): A modelling study, *J. Marine Syst.*, 81, 75–85,  
1039 <https://doi.org/10.1016/j.jmarsys.2009.12.003>, 2010.
- 1040
- 1041 Legendre, L., Ackley, S. F., Dieckmann, G. S., Gulliksen, B., Horner, R., Hoshiai, T., Melnikov, I. A., Reebergh, W.  
1042 S., Spindler, M., and Sullivan, C. W.: Ecology of sea ice biota: 2. Global significance, *Polar Biol.*, 12, 429–444,  
1043 <https://doi.org/10.1007/bf00243114>, 1992.
- 1044
- 1045 Lellouche, J.-M., Greiner, E., Le Galloudec, O., Garric, G., Regnier, C., Drevillon, M., Benkiran, M., Testut, C.-E.,  
1046 Bourdalle-Badie, R., Gasparin, F., Hernandez, O., Levier, B., Drillet, Y., Remy, E., and Le Traon, P.-Y. : Recent  
1047 updates to the Copernicus Marine Service global ocean monitoring and forecasting real-time 1/12° high-resolution  
1048 system, *Ocean Sci.*, 14, 1093–1126, <https://doi.org/10.5194/os-14-1093-2018>, 2018.
- 1049
- 1050 Lellouche, J.-M., Greiner, E., Bourdallé-Badie, R., Garric, G., Melet, A., Drévillon, M., Clement, B., Hamon, M., Le  
1051 Galloudec, O., Regnier, C., Candela, T., Testut, C.-E., Gasparin, F., Ruggiero, G., Mounir, B., Yann, D., and Le  
1052 Traon, P.-Y. : The Copernicus Global 1/12° Oceanic and Sea Ice GLORYS12 Reanalysis, *Front. Earth Sci.*, 9,  
1053 698876, <https://doi.org/10.3389/feart.2021.698876>, 2021.
- 1054
- 1055 Lipscomb, W. H. and Hunke, E. C.: Modeling sea ice transport using incremental mapping, *Mon. Weather Rev.*,  
1056 132(6), 1341–1354, [https://doi.org/10.1175/1520-0493\(2004\)132%3C1341:MSITUI%3E2.0.CO;2](https://doi.org/10.1175/1520-0493(2004)132%3C1341:MSITUI%3E2.0.CO;2), 2004.
- 1057
- 1058 Lu, Y., Higginson, S., Nudds, S., Prinsenber, S., and Garric, G.: Model simulated volume fluxes through the  
1059 Canadian Arctic Archipelago and Davis Strait: Linking monthly variations to forcings in different seasons, *J.*  
1060 *Geophys. Res.-Oceans*, 119, 1927–1942, <https://doi.org/10.1002/2013JC009408>, 2014.
- 1061
- 1062 Ma, Z., Han, G., and Chassé, J.: Simulation of circulation and ice over the Newfoundland and Labrador Shelves:  
1063 The mean and seasonal cycle, *Atmos.-Ocean*, 54(3), 248–263, <https://doi.org/10.1080/07055900.2015.1077325>,  
1064 2016.
- 1065
- 1066 Marchesiello, P., McWilliams, J. C., and Shchepetkin, A.: Open boundary conditions for long-term integration of  
1067 regional oceanic models, *Ocean Model.*, 3, 1–20, [https://doi.org/10.1016/S1463-5003\(00\)00013-5](https://doi.org/10.1016/S1463-5003(00)00013-5), 2001.
- 1068
- 1069 Marchesiello, P., Debreu, L., Couvelard, X.: Spurious diapycnal mixing in terrain-following coordinate models: The  
1070 problem and a solution, *Ocean Model.*, 26, 156–169, <https://doi.org/10.1016/j.ocemod.2008.09.004>, 2009.
- 1071
- 1072 Martz, T. R., DeGrandpre, M. D., Strutton, P. G., McGillis, W. R., and Drennan, W. M.: Sea surface pCO<sub>2</sub> and  
1073 carbon export during the Labrador Sea spring-summer bloom: An in situ mass balance approach, *J. Geophys. Res.*,  
1074 114, C09008, <https://doi.org/10.1029/2008JC005060>, 2009.
- 1075
- 1076 Mason, E., Molemaker, J., Shchepetkin, A. F., Colas, F., McWilliams, J. C., and Sangrà, P.: Procedures for offline  
1077 grid nesting in regional ocean models, *Ocean Model.*, 35, 1–15, <https://doi.org/10.1016/j.ocemod.2010.05.007>,  
1078 2010.
- 1079
- 1080 McDougall, T. M. and Barker, P. M.: Getting started with TEOS-10 and the Gibbs Seawater (GSW) Oceanographic  
1081 Toolbox, SCOR/IAPSO WG127, ISBN 978-0-646-55621-5, 2011.
- 1082
- 1083 Melsheimer, C. and Spreen, G.: AMSR2 ASI sea ice concentration data, Arctic, version 5.4 (NetCDF) (June 2012 -  
1084 December 2018) [data set], PANGAEA, <https://doi.org/10.1594/PANGAEA.898399>, 2019.
- 1085



- 1086 Mellor, G. L. and Yamada, T.: Development of a turbulence closure model for geophysical fluid problems, *Rev.*  
1087 *Geophys. and Space Phys.*, 20(4), 851–875, <https://doi.org/10.1029/RG020i004p00851>, 1982.  
1088
- 1089 Mysak, L. A., Peng, S., and Wood, R. G.: Application of a coupled ice-ocean model to the Labrador Sea, *Atmos.-*  
1090 *Ocean*, 29(2), 232–255, <https://doi.org/10.1080/07055900.1991.9649404>, 1991.  
1091
- 1092 Naughten, K. A., Galton-Fenzi, B. K., Meissner, K. J., England, M. H., Brassington, G. B., Colberg, F., Hatterman,  
1093 T., and Debernard, J. B.: Spurious sea ice formation caused by oscillatory ocean tracer advection schemes, *Ocean*  
1094 *Model.*, 116, 108–117, <https://doi.org/10.1016/j.ocemod.2017.06.010>, 2017.  
1095
- 1096 Ohashi, K., Laurent, A., Renkl, C., Sheng, J., Fennel, K., and Oliver, E.: DALROMS-NWA12 v1.0, a coupled  
1097 circulation-sea ice-biogeochemistry model for the northwest North Atlantic: codes and namelists (Version v3)  
1098 [software], Zenodo, <https://doi.org/10.5281/zenodo.12752091>, 2024a.  
1099
- 1100 Ohashi, K., Laurent, A., Renkl, C., Sheng, J., Fennel, K., and Oliver, E.: DALROMS-NWA12 v1.0, a coupled  
1101 circulation-sea ice-biogeochemistry model for the northwest North Atlantic: input files (1 of 3) (Version v2) [data  
1102 set], Zenodo, <https://doi.org/10.5281/zenodo.12752190>, 2024b.  
1103
- 1104 Ohashi, K., Laurent, A., Renkl, C., Sheng, J., Fennel, K., and Oliver, E.: DALROMS-NWA12 v1.0, a coupled  
1105 circulation-sea ice-biogeochemistry model for the northwest North Atlantic: input files (2 of 3) (Version v1) [data  
1106 set], Zenodo, <https://doi.org/10.5281/zenodo.12734049>, 2024c.  
1107
- 1108 Ohashi, K., Laurent, A., Renkl, C., Sheng, J., Fennel, K., and Oliver, E.: DALROMS-NWA12 v1.0, a coupled  
1109 circulation-sea ice-biogeochemistry model for the northwest North Atlantic: input files (3 of 3) (Version v1) [data  
1110 set], Zenodo, <https://doi.org/10.5281/zenodo.12735153>, 2024d.  
1111
- 1112 Ohashi, K., Laurent, A., Renkl, C., Sheng, J., Fennel, K., and Oliver, E.: DALROMS-NWA12 v1.0, a coupled  
1113 circulation-sea ice-biogeochemistry model for the northwest North Atlantic: output files (1 of 2) (Version v1) [data  
1114 set], Zenodo, <https://doi.org/10.5281/zenodo.12744506>, 2024e.  
1115
- 1116 Ohashi, K., Laurent, A., Renkl, C., Sheng, J., Fennel, K., and Oliver, E.: DALROMS-NWA12 v1.0, a coupled  
1117 circulation-sea ice-biogeochemistry model for the northwest North Atlantic: output files (2 of 2) (Version v1) [data  
1118 set], Zenodo, <https://doi.org/10.5281/zenodo.12746262>, 2024f.  
1119
- 1120 Pei, Q.: Study of circulation, hydrography and dissolved oxygen concentration over coastal waters of the Scotian  
1121 Shelf, M.Sc. thesis, Dalhousie University, <http://hdl.handle.net/10222/81682>, 2022.  
1122
- 1123 Pennelly, C. and Myers, P. G.: Introducing LAB60: A 1/60° NEMO 3.6 numerical simulation of the Labrador Sea,  
1124 *Geosci. Model Dev.*, 13, 4959–4975, <https://doi.org/10.5194/gmd-13-4959-2020>, 2020.  
1125
- 1126 Pepin, P., Petrie, B., Therriault, J.-C., Narayanan, S., Harrison, W. G., Frank, K. T., Chassé, J., Colbourne, E. B.,  
1127 Gilbert, D., Gregory, D., Harvey, M., Maillet, G. L., Mitchell, M., and Starr, M.: The Atlantic Zone Monitoring  
1128 Program (AZMP): Review of 1998–2003 (*Can. Tech. Rep. Hydrogr. Ocean Sci.* 242), Fisheries and Oceans  
1129 Canada, 2005.  
1130
- 1131 Prinsenberg, S. J. and Peterson, I. K.: Sea-ice properties off Labrador and Newfoundland during LIMEX '89,  
1132 *Atmos.-Ocean*, 30(2), 207–222, <https://doi.org/10.1080/07055900.1992.9649438>, 1992.  
1133
- 1134 Richaud, B., Fennel, K., Oliver, E. C. J., DeGrandpre, M. D., Bourgeois, T., Hu, X., and Lu, Y.: Underestimation of  
1135 oceanic carbon uptake in the Arctic Ocean: ice melt as predictor of the sea ice carbon pump, *Cryosphere*, 17,  
1136 2665–2680, <https://doi.org/10.5194/tc-17-2665-2023>, 2023.  
1137
- 1138 Richaud, B., Kwon, Y.-O., Joyce, T. M., Fratantoni, P. S., and Lentz, S. J.: Surface and bottom temperature and  
1139 salinity climatology along the continental shelf off the Canadian and U.S. east coasts, *Cont. Shelf Res.*, 124, 165–  
1140 181, <https://doi.org/10.1016/j.csr.2016.06.005>, 2016.  
1141



- 1142 Ridenour, N. A., Hu, X., Sydor, K., Myers, P. G., and Barber, D. G.: Revisiting the circulation of Hudson Bay:  
1143 Evidence for a seasonal pattern, *Geophys. Res. Lett.*, 46, 3891–3899, <https://doi.org/10.1029/2019GL082344>,  
1144 2019.  
1145
- 1146 Ross, A. C., Stock, C. A., Adcroft, A., Curchitser, E., Hallberg, R., Harrison, M. J., Hedstrom, K., Zadeh, N.,  
1147 Alexander, M., Chen, W., Drenkard, E. J., du Pontavice, H., Dussin, R., Gomez, F., John, J. G., Kang, D., Lavoie,  
1148 D., Resplandy, L., Roobaert, A., Saba, V., Shin, S., Siedlecki, S., and Simkins, J.: A high-resolution physical-  
1149 biological model for marine resource applications in the northwest Atlantic (MOM6-COBALT-NWA12 v1.0),  
1150 *Geosci. Model Dev.*, 16, 6943–6985, <https://doi.org/10.5194/gmd-16-6943-2023>, 2023.  
1151
- 1152 Rutherford, K. and Fennel, K.: Elucidating coastal ocean carbon transport processes: A novel approach applied to  
1153 the northwest North Atlantic shelf, *Geophys. Res. Lett.*, 49, e2021GL097614,  
1154 <https://doi.org/10.1029/2021GL097614>, 2022.  
1155
- 1156 Saucier, F. J., Senneville, S., Prinsenber, S., Roy, F., Smith, G., Gachon, P., Caya, D., and Laprise, R.: Modelling  
1157 the sea ice-ocean seasonal cycle in Hudson Bay, Foxe Basin and Hudson Strait, Canada, *Clim. Dynam.*, 23, 303–  
1158 326, <https://doi.org/10.1007/s00382-004-0445-6>, 2004.  
1159
- 1160 Schwab, D. J., Clites, A. H., Murthy, C. R., Sandall, J. E., Meadows, L. R., and Meadows, G. A.: The effect of wind  
1161 on transport and circulation in Lake St. Clair, *J. Geophys. Res.*, 94(C4), 4947–4958,  
1162 <https://doi.org/10.1029/JC094iC04p04947>, 1989.  
1163
- 1164 Shapiro, R.: Linear filtering, *Math. Comput.*, 19(132), 1094–1097, <https://doi.org/10.1090/S0025-5718-1975-0389356-X>, 1975.  
1165  
1166
- 1167 Sheng, J.: Circulation and drift pathways in the northwest Atlantic Ocean, in: *Estuarine and Coastal Modeling:*  
1168 *Proceedings of the Seventh International Conference*, St. Petersburg, FL, 5–7 November 2001, 364–383,  
1169 [https://doi.org/10.1061/40628\(268\)23](https://doi.org/10.1061/40628(268)23), 2002.  
1170
- 1171 Smith, G. C., Roy, F., and Brasnett, B.: Evaluation of an operational ice-ocean analysis and forecasting system for  
1172 the Gulf of St. Lawrence, *Q. J. Roy. Meteor. Soc.*, 139, 419–433, <https://doi.org/10.1002/qj.1982>, 2013.  
1173
- 1174 Song, Y. and Haidvogel, D.: A semi-implicit ocean circulation model using a generalized topography-following  
1175 coordinate system. *J. Comput. Phys.*, 115(1), 228–244, <https://doi.org/10.1006/jcph.1994.1189>.  
1176
- 1177 St. Lawrence Global Observatory: Freshwater runoffs of the St. Lawrence at the height of Québec City [data set],  
1178 [https://catalogue.ogs.l.ca/dataset/ca-cioos\\_84a17ffc-4898-4261-94de-4a5ea2a9258d?local=en](https://catalogue.ogs.l.ca/dataset/ca-cioos_84a17ffc-4898-4261-94de-4a5ea2a9258d?local=en), 2023.  
1179
- 1180 Strutton, P. G., Martz, T. R., DeGrandpre, M. D., McGillis, W. R., Drennan, W. M., and Boss, E.: Bio-optical  
1181 observations of the 2004 Labrador Sea phytoplankton bloom, *J. Geophys. Res.*, 116, C11037,  
1182 <https://doi.org/10.1029/2010JC006872>, 2011.  
1183
- 1184 Szekely, T.: Product user manual: In situ TAC objective analysis products, v1.11, Mercator Ocean International,  
1185 2023.  
1186
- 1187 Takahashi, T., Sutherland, S. C., Wanninkhof, R., Sweeney, C., Feely, R.A., Chipman, D. W., Hales, B., Friederich,  
1188 G., Chavez, F., Sabine, C., Watson, A., Bakker, D. C. E., Schuster, U., Metzl, N., Yoshikawa-Inoue, H., Ishii, M.,  
1189 Midorikawa, T., Nojiri, Y., Körtzinger, A., Steinhoff, T., Hoppema, M., Olafsson, J., Arnarson, T. S., Tilbrook, B.,  
1190 Johannessen, T., Olsen, A., Bellerby, R., Wong, C. S., Delille, B., Bates, N. R., de Barr, H. J. W., Climatological  
1191 mean and decadal change in surface ocean pCO<sub>2</sub>, and net sea-air CO<sub>2</sub> flux over the global oceans, *Deep-Sea Res.*  
1192 *Pt. II*, 56, 554–577, <https://doi.org/10.1016/j.dsr2.2008.12.009>, 2009.  
1193
- 1194 Tang, C. L., Gui, Q., and DeTracey, B. M.: A modeling study of upper ocean winter processes in the Labrador Sea, *J.*  
1195 *Geophys. Res.*, 104(C10), 23411–23425, <https://doi.org/10.1029/1999JC900214>, 1999.  
1196



- 1197 The Lab Sea Group: The Labrador Sea Deep Convection Experiment, *B. Am. Meteorol. Soc.*, 79(10), 2033–2058,  
1198 [https://doi.org/10.1175/1520-0477\(1998\)079%3C2033:TLSDCE%3E2.0.CO;2](https://doi.org/10.1175/1520-0477(1998)079%3C2033:TLSDCE%3E2.0.CO;2), 1998.  
1199
- 1200 Thyng, K. M., Greene, C. A., Hetland, R. D., Zimmerle, H. M., and DiMarco, S. F.: True colors of oceanography:  
1201 Guidelines for effective and accurate colormap selection. *Oceanography*, 29(3), 9–13,  
1202 <https://doi.org/10.5670/oceanog.2016.66>, 2016.  
1203
- 1204 Tian, R. C., Deibel, D., Rivkin, R. B., and Vézina, A. F.: Biogenic carbon and nitrogen export in a deep-convection  
1205 region: simulations in the Labrador Sea, *Deep-Sea Res. Pt. I*, 51, 413–437,  
1206 <https://doi.org/10.1016/j.dsr.2003.10.015>, 2004.  
1207
- 1208 Urrego-Blanco, U., and Sheng, J.: Study on subtidal circulation and variability in the Gulf of St. Lawrence, Scotian  
1209 Shelf, and Gulf of Maine using a nested-grid shelf circulation model, *Ocean Dynam.*, 64, 385–412,  
1210 <https://doi.org/10.1007/s10236-013-0688-z>, 2014.  
1211
- 1212 Volk, T. and Hoffert, M. I.: Ocean carbon pumps: Analysis of relative strengths and efficiencies in ocean-driven  
1213 atmospheric CO<sub>2</sub> changes, in: *The carbon cycle and atmospheric CO<sub>2</sub>: Natural variations Archean to present*,  
1214 *Geoph. Monog. Series vol. 32*, edited by Sundquist, E. T. and Broecker, W. S., 99–110,  
1215 <https://doi.org/10.1029/GM032p0099>, 1985.  
1216
- 1217 Wang, B., Fennel, K., An assessment of vertical carbon flux parameterizations using backscatter data from BGC  
1218 Argo, *Geophys. Res. Lett.*, <https://doi.org/10.1029/2022GL101220>, 2023.  
1219
- 1220 Wang, B., Fennel, K., Biogeochemical Argo data suggest only a minor contribution of small particles to long-term  
1221 carbon sequestration in the subpolar North Atlantic, *Limnol. Oceanogr.*, <https://doi.org/10.1002/lno.12209>, 2022.  
1222
- 1223 Wang, Y., Sheng, J., and Lu, Y.: Examining tidal impacts on seasonal circulation and hydrography variability over  
1224 the eastern Canadian shelf using a coupled circulation-ice regional model, *Prog. Oceanogr.*, 189, 102448,  
1225 <https://doi.org/10.1016/j.pocean.2020.102448>, 2020.  
1226
- 1227 Wang, Z., Lu, Y., Greenan, B., Brickman, D., and DeTracey, B.: BNAM: An eddy-resolving North Atlantic Ocean  
1228 model to support ocean monitoring. (Can. Tech. Rep. Hydrogr. Ocean Sci. 327), Fisheries and Oceans Canada,  
1229 2018.  
1230
- 1231 Wu., Y., Peterson, I. K., Tang, C. C. L., Platt, T., Sathyendranath, S., and Fuentes-Yaco, C.: The impact of sea ice on  
1232 the initiation of the spring bloom on the Newfoundland and Labrador Shelves, *J. Plankton. Res.*, 29(6), 509–514,  
1233 <https://doi.org/10.1093/plankt/fbm035>, 2007.  
1234
- 1235 Wu, Y., Platt, T., Tang, C. C. L., and Sathyendranath, S.: Regional differences in the timing of the spring bloom in  
1236 the Labrador Sea, *Mar. Ecol. Prog. Ser.*, 355, 9–20, <https://doi.org/10.3354/meps07233>, 2008.  
1237
- 1238 Wu, Y., Tang, C., and Hannah, C.: The circulation of eastern Canadian seas, *Prog. Oceanogr.*, 106, 28–48,  
1239 <https://doi.org/10.1016/j.pocean.2012.06.005>, 2012.  
1240
- 1241 Wu, H. and Zhu, J.: Advection scheme with 3rd high-order spatial interpolation at the middle temporal level and its  
1242 application to saltwater intrusion in the Changjiang Estuary, *Ocean Model.*, 33(1–2), 33–51,  
1243 <https://doi.org/10.1016/j.ocemod.2009.12.001>, 2010.  
1244
- 1245 Yang, B., Fox, J., Behrenfeld, M. J., Boss, E. S., Haëntjens, N., Halsey, K. H., Emerson, S. R., and Doney, S. C.: In  
1246 situ estimates of net primary production in the western North Atlantic with Argo profiling floats, *J. Geophys.*  
1247 *Res.-Biogeo.*, 126, e2020JG006116, <https://doi.org/10.1029/2020JG006116>, 2020.  
1248
- 1249 Yang, S., Sheng, J., Ohashi, K., Yang, B., Chen, S., Xing, J.: Non-linear interactions between tides and storm surges  
1250 during extreme weather events over the eastern Canadian shelf, *Ocean Dynam.*, 73, 279–301,  
1251 <https://doi.org/10.1007/s10236-023-01556-w>, 2023.  
1252



- 1253 Yao, T., Tang, C. L., and Peterson, I. K.: Modeling the seasonal variation of sea ice in the Labrador Sea with a  
1254 coupled multcategory ice model and the Princeton Ocean Model, *J. Geophys. Res.*, 105(C1), 1153–1165,  
1255 <https://doi.org/10.1029/1999JC900264>, 2000.  
1256
- 1257 Yashayaev, I. and Loder, J. W.: Further intensification of deep convection in the Labrador Sea in 2016, *Geophys.*  
1258 *Res. Lett.*, 44(3), 1429–1438, <https://doi.org/10.1002/2016GL071668>, 2017.  
1259
- 1260 Zhang, S., Sheng, J., and Greatbatch, R. J.: A coupled ice-ocean modeling study of the northwest Atlantic Ocean, *J.*  
1261 *Geophys. Res.*, 109, C04009, <https://doi.org/10.1029/2003JC001924>, 2004.  
1262